The Structure and Propagation of Intraseasonal Oscillations Appearing in a GFDL General Circulation Model

NGAR-CHEUNG LAU

Geophysical Fluid Dynamics Laboratory/NOAA, Princeton University, Princeton, NJ 08542

KA-MING LAU

Goddard Laboratory for Atmospheres, NASA/Goddard Space Flight Center, Greenbelt, MD 20771

(Manuscript received 22 November 1985, in final form 17 March 1986)

ABSTRACT

The three-dimensional structure and temporal evolution of quasi-periodic, planetary-scale tropospheric oscillations simulated by a 15-wavenumber GCM are investigated by applying cross-spectral, eigenvector, composite and temporal correlation techniques to 12 years of model output. Evident from this diagnostic study is the presence in the model tropics of well-defined eastward traveling features with spatial scales of zonal wavenumbers 1 and 2, and with temporal scales of 25–40 and 15–20 days, respectively. The flow pattern associated with the oscillations of both spatial scales is characterized by circulation cells oriented along the equatorial zonal plane, with the zonal wind and geopotential height fluctuations near the sea level being negatively correlated with the corresponding fluctuations in the upper troposphere. The movement of these zonal circulation cells along the equatorial belt is accompanied by systematic migration of the global-scale horizontal divergence field, and by dipole-like precipitation structures within the Indonesian/Pacific sector. The preferred sites for such oscillatory behavior exhibit a notable seasonal dependence, with the most active zonal circulation cells being located in the summer hemisphere.

During the northern summer, the 25–40 day oscillations coincide with the occurrence of northward moving, zonally elongated rainbands over the monsoon region of South Asia. During the northern winter, the 25–40 day phenomena in the tropics are linked to well-organized extratropical wave trains spanning the Eurasian and Pacific/North American sectors.

The principal characteristics of the model-generated phenomena analyzed in this study are compared with corresponding results reported in the observational literature. Although the period of the simulated wavenumber-1 phenomena is somewhat shorter than the corresponding observed values, it is demonstrated that the spatial structure, propagation characteristics and seasonal dependence of the model features are consistent with observations. The model findings are also interpreted in terms of current theoretical understanding of tropical and extratropical motions.

1. Introduction

The nature of quasi-periodic phenomena in the atmosphere has long been a subject of considerable scientific interest to the meteorological community. Special attention has recently been devoted to tropospheric oscillations with time scales ranging from about 10 days to a season, not only because these phenomena seem to be linked to a variety of fundamental dynamical and physical processes, but also in view of the potential impact of these circulation features on extended-range weather prediction.

Signals of a well-defined tropical oscillation with a 40–50 day period were detected by Madden and Julian (1971, 1972) using long observational records at selected rawinsonde stations. This global-scale oscillation takes the form of eastward moving circulation cells in the equatorial zonal plane. Accompanying the movement of these circulation cells are temporally and spatially coherent fluctuations in surface pressure, as well as zonal wind in the upper and lower troposphere.

With the advent of routine monitoring of the tropical atmosphere by meteorological satellites, as well as the availability of synoptic analyses covering the entire globe, investigations of tropical oscillations with intraseasonal times scales were given added impetus. Contemporary studies suggest that the observed phenomena are characterized by a rather broad frequency response, with comparable power in time periods ranging from 30 to 60 days. However, in conformity with the terminology commonly used in the established literature, we shall still refer to these observed features as the "40–50 day oscillations."

It is now known that the 40–50 day oscillations occur throughout the year. For instance, Maruyama (1982) analyzed cloud wind vectors derived from satellite measurements over the tropical Pacific, and found prominent spectral peaks in the upper tropospheric zonal wind within the 30–50 day band in all seasons. The 40–50 day oscillations have also been studied using data for the FGGE year (December 1978–November 1979), when intense efforts were made to monitor the

atmospheric circulation over the whole globe. By examining the velocity potential field, which depicts the planetary-scale divergent flow, Lorenc (1984) reported the presence in the entire FGGE period of eastward moving phenomena with zonal wavenumbers 1 and 2, and with periods of 30–50 and 5–15 days, respectively.

The seasonal characteristics of the 40–50 day oscillations have been the subject of several investigations. Sardeshmukh and Hoskins (1985) noted a strong 40–50 day signal in the 150 mb divergence field over the central equatorial Pacific during the northern winter of 1982/83. The spatial pattern and propagation characteristics of Northern Hemisphere wintertime convective activity within the 40–50 day band were also examined by Lau and Chan (1985), using a multiyear outgoing longwave radiation (OLR) data set for the tropical Pacific and Indian Oceans. Their analyses reveal that the OLR anomalies appear as eastward propagating dipoles oriented in the zonal direction. The propagation speed of these features is seen to exhibit a notable geographical dependence.

The 40–50 day oscillations are also associated with interesting circulation features during the northern summer. The FGGE study performed by Lorenc (1984) indicates that the temporal phase of such oscillations is apparently linked to the onset, break, revival and final withdrawal of the summer monsoon over South Asia. The local circulation accompanying these distinct stages of monsoon activity is characterized by northward migrating belts of anomalous divergence and convergence. These findings are substantiated by the diagnostic studies based on FGGE data (Krishnamurti and Subrahmanyam, 1982; Krishnamurti et al., 1985; Murakami and Nakazawa, 1985). The meridional movement of convective activity associated with the active-break monsoon cycles has also been reported by Yasunari (1979, 1980) using satellite mosaic pictures of cloudiness over South Asia. Analogous features have also been identified by Knutson et al. (1986) and Lau and Chan (1986) on the basis of OLR data for several northern summers.

Observational studies of atmospheric variability in the extratropics (e.g., Blackmon, 1976) indicate that a large fraction of the intraseasonal variability resides in the 10–90 day period range. It is hence important to discern the relationships between tropical 40–50 day oscillations and midlatitude fluctuations of comparable time scales. The observed spatial structure and propagation characteristics of slowly varying extratropical phenomena have been described by Blackmon et al. (1984a, 1984b) in terms of Rossby wave trains and geographically fixed standing oscillations. The extent to which these fluctuations are linked to localized tropical convection were explored by Liebmann and Hartmann (1984) on the basis of OLR and 500 mb height data for northern winter. These authors have noted considerable tropical–midlatitude interaction on intraseasonal time scales.

The association between tropical and extratropical circulations within the specific framework of 30–60 day oscillations was studied by Weickmann et al. (1985). By analyzing Northern Hemispheric wintertime OLR and 250 mb wind data for the past decade, they have documented several relationships between the planetary-scale extratropical flow and tropical convection during a complete life cycle of these oscillations. Lau and Phillips (1986) examined the coherent variations of the 500 mb height field associated with different OLR distributions on 40–50 day time scales during the northern winter. They found that the extratropical wave trains over Eurasia and Pacific/North America are phase-locked to an eastward propagating dipole-like OLR anomaly over the tropical Indian and western Pacific Oceans.

Thus a firm observational basis has been established for various aspects of these 40–50 day oscillations. At present, a complete theoretical understanding of this global-scale phenomenon is being actively sought by various investigators. One useful contribution to this ongoing endeavor is to determine whether the essential properties of these oscillations can be reproduced under the controlled setting of numerical models. A natural candidate for making such a determination would be a current version of a comprehensive general circulation model (GCM), which incorporates many of the known dynamical and physical processes governing the large-scale atmospheric behavior. Upon demonstrating that the 40–50 day oscillations are indeed present in GCM simulations, it might then be feasible to identify the essential mechanisms associated with this phenomenon in the model atmosphere.

Hence the primary objective of the present study is to document the nature of oscillations with intraseasonal time scales appearing in the 12-year duration of a GCM experiment performed at the Geophysical Fluid Dynamics Laboratory (GFDL). Much of the model diagnosis is aimed at delineating the three-dimensional spatial structure, frequency dependence and propagation characteristics of the simulated oscillations. Evidence will also be shown on the connection between the oscillatory behavior in the tropics and the monsoon activity over South Asia in the summer, as well as the coincidence of the tropical oscillations with midlatitude wave motions in the northern winter. Throughout this presentation, comparisons between the model features and observational results are emphasized.

The methodology adopted in the present study is summarized as follows. The presence of coherent propagating oscillations in the model tropics is first ascertained using cross-spectral and empirical orthogonal function analyses (sections 3 and 4). The periods when the principal oscillatory mode attain high amplitudes are then identified, and the detailed structure of these phenomena as they evolve through a complete life cycle is described using composite charts and Hovmöller diagrams (section 5). Seasonal character-

istics of these tropical oscillations are examined in terms of their relationships with the Asian summer monsoon and with wintertime extratropical flow, and seasonal displacements in the preferred regions of occurrence are illustrated using charts of correlation statistics (section 6). Next, the properties of oscillations explaining a lesser fraction of the total variance are analyzed (section 7). Finally, some dynamical interpretations of the model results are offered (section 8).

2. Model description and data analysis procedures

The model integration examined in this study is the same as that analyzed earlier by Manabe and Hahn (1981) and Lau (1981), who have provided a detailed compilation of the model formulation and climatology. The GCM used for this integration is a 9-level, 15-wavenumber spectral model with realistic distributions of continents and orography. Incorporated in this model is a comprehensive physics package containing radiative transfer processes, ground hydrology, moist convective adjustment and ice-albedo feedback. The cloud cover is prescribed to be a function of latitude and height only. The model experiment has been performed for a total duration of 17.75 years. In the course of the integration, various boundary conditions such as sea surface temperature and solar heating were constrained to evolve through successive annual cycles which are identical to each other; thus, no interannual variability has been introduced to the external forcing of the model environment.

The database for the present study is extracted from the history tapes for a 12-year period in the integration described above. The meteorological variables analyzed include 5-day averages of the horizontal wind at 830 and 205 mb, geopotential height at 830, 515 and 205 mb, sea level pressure and precipitation. The climatological seasonal cycle has been removed from these individual time series prior to further processing.

In order to retain fluctuations with periods lying within specific ranges, two 41-point digital filters have been designed. The methodology for applying these time filters is similar to that described by Blackmon (1976), except that the filters used here consist of 21 coefficients and the time series being processed consist of 5-day means. The coefficients associated with these filters are listed in Table 1, and the corresponding frequency response for data values sampled at 5-day intervals is illustrated in Fig. 1. The first filter yields a peak response for the band with periods between about 16 and 45 days, and is hereafter referred to as the "bandpass" filter. The second filter mostly retains fluctuations with periods shorter than 25 days, and will be referred to as the "high pass" filter.

TABLE 1. Coefficients a_p of the 41-point digital band pass and high pass filters used in this study.

Coefficients	Filters*	
	Band pass	High pass
a_0	0.5000000000	0.6666666667
a_1	0.1160969239	−0.2746882708
a_2	−0.2717748224	−0.1358874115
a_3	−0.1027564348	0.0000000001
a_4	0.0000000000	0.0650862179
a_5	−0.0794996326	0.0504007477
a_6	−0.0000000001	−0.0000000001
a_7	0.0519852945	−0.0329573559
a_8	0.0000000000	−0.0272575620
a_9	0.0262163892	0.0000000001
a_{10}	0.0379459456	0.0189729726
a_{11}	−0.0067028244	0.0158590530
a_{12}	−0.0000000001	−0.0000000001
a_{13}	0.0046403796	0.0109792558
a_{14}	−0.0181030363	−0.0090515183
a_{15}	−0.0085363981	0.0000000001
a_{16}	0.0000000000	0.0059648059
a_{17}	−0.0074731487	0.0047377865
a_{18}	−0.0000000000	0.0000000000
a_{19}	0.0044067184	−0.0027937475
a_{20}	0.0000000000	−0.0020394394

* The filtered data at time t_i, $[\tilde{c}(t_i)]$, are obtained from the unfiltered 5-day means $[c(t_{i-20}), \ldots, c(t_{i+20})]$ by $\tilde{c}(t_i) = a_0 c(t_i) + \sum_{p=1}^{20} a_p[c(t_{i-p}) + c(t_{i+p})]$.

3. Cross-spectral analysis

The propagation characteristics of quasi-periodic phenomena may be discerned using cross-spectral techniques, which yield the frequency dependence of the phase and coherence between fluctuations at different locations. In the present study, these spectral quantities are obtained by applying the lag-correlation method to the unfiltered time series of 5-day averages, with the number of lags being set equal to 10. Figure 2 shows the phase differences between fluctuations at the reference grid point 2.25°S, 180°E (denoted in all panels by a solid dot) and the corresponding fluctuations at all remaining grid points within the tropical belt. The phase patterns shown in Fig. 2 have been constructed using spectral estimates for the frequency band corresponding to a time period of 25 days. Additional computations (not shown) indicate that patterns qualitatively similar to those in Fig. 2 may be obtained for various bands with periods ranging from about 20 to 40 days. The meteorological fields being analyzed in this manner are the velocity potential at a) 205 and b) 830 mb, which depict, respectively, the global-scale horizontal divergence in the upper and lower troposphere; c) zonal wind at 205 mb; and d) sea level pressure.

The phase information is represented by the orientation of the arrows with the following convention: Those points with fluctuations which are exactly in phase with the reference point are indicated by northward pointing arrows. The arrows are rotated in a clockwise fashion if the transient fluctuations at the

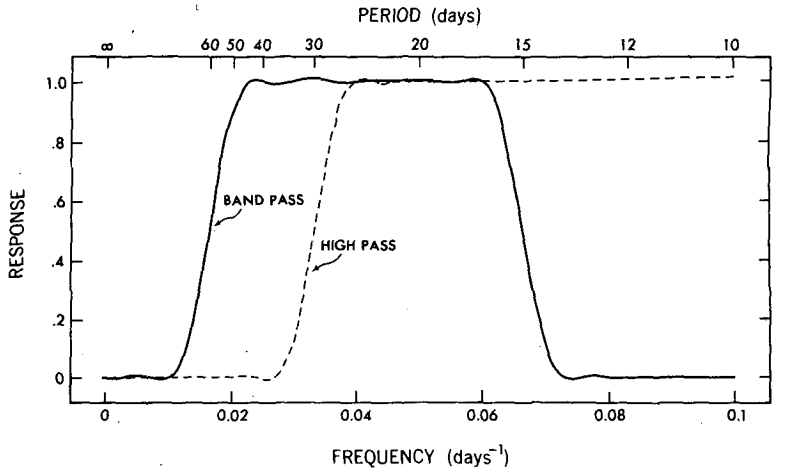

FIG. 1. Frequency response of the bandpass (solid curve) and high pass (dashed curve) filters used in this study.

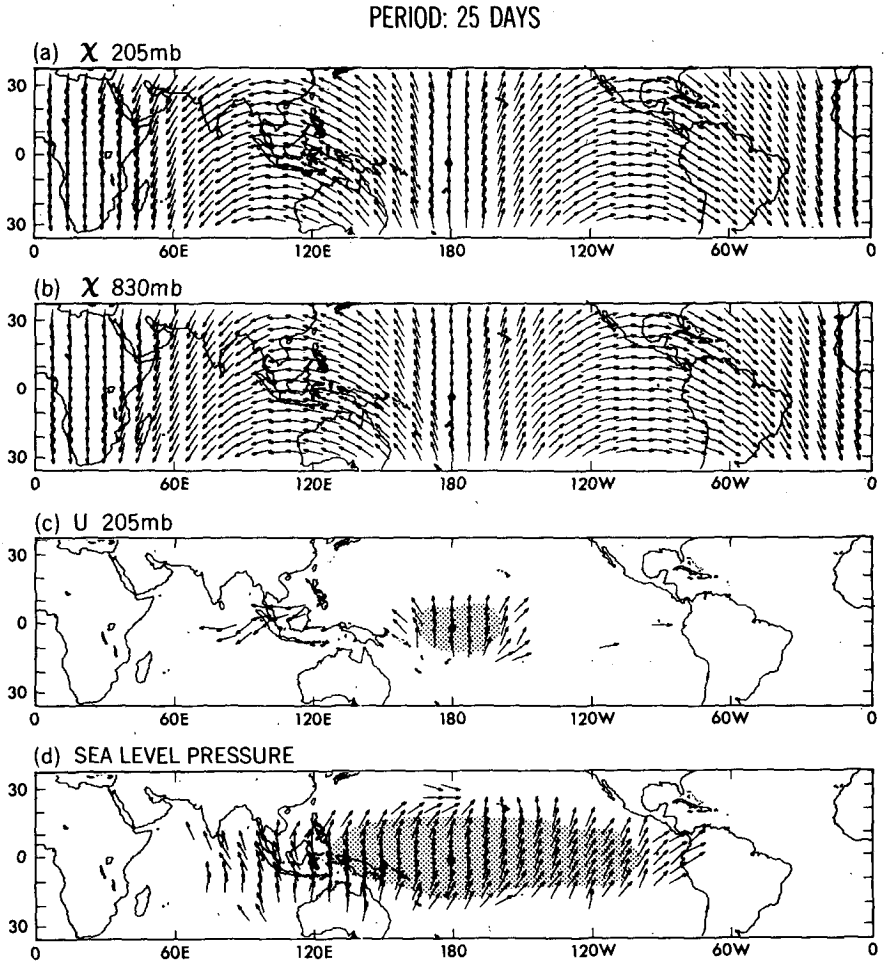

FIG. 2. Distributions of phase differences between fluctuations at individual grid points and fluctuations at the reference point (2.25°S, 180°E, indicated by a solid dot in each panel) for the spectral band centered at a period of 25 days, as computed using unfiltered 5-day averages of (a) 205 mb velocity potential, (b) 830 mb velocity potential, (c) 205 mb zonal wind and (d) sea level pressure for the entire 12-year period. Arrows pointing due north indicate zero phase difference. Arrows are rotated in a clockwise (counterclockwise) fashion by 1° for each degree of phase lag (lead) relative to the reference point. See text for further details. Arrows are not plotted over locations with squared coherence values less than 0.05. The squared coherence values exceed the 95% significance level at all grid points in panels (a) and (b), and only at those grid points covered by shading in panels (c) and (d).

point in question lag those at the reference point. Conversely, locations with disturbances leading the reference point are indicated by a counterclockwise rotation of the arrows. The arrows rotate by 1° for each degree of phase difference. For example, southward pointing arrows indicate locations where the fluctuations are 180° out of phase relative to the reference point, eastward pointing arrows indicate phase lags of 90°, westward pointing arrows indicate phase leads of 90°, and so forth.

The confidence level may be assessed by computing the coherence statistics. In Fig. 2, the phase information is plotted only over those locations with squared coherence larger than 0.05. Standard statistical tests (e.g., Panofsky and Brier, 1958; Julian, 1975) indicate that the squared coherence values for the velocity potential fields (Fig. 2a, b) exceed the 95% significance level throughout the entire tropical belt. The coherence levels for the 205 mb zonal wind (Fig. 2c) and sea level pressure (Fig. 2d) are comparatively lower, and shading is used in these two panels to indicate those locations where the 95% limit (i.e., squared coherence larger than 0.18) is surpassed.

Figure 2a,b is characterized by a continuous clockwise rotation of the phase arrows as one traverses from west to east, thus indicating a systematic eastward propagation of velocity potential fluctuations with rather uniform phase speeds. It is also evident that the arrows rotate through a 360° cycle for each complete circuit around the tropical belt. The dominant spatial scale for these traveling disturbances is hence seen to be zonal wavenumber 1.

Although the phase patterns for 205 mb zonal wind and sea level pressure (Fig. 2c, d) are less coherent, it is still possible to discern the eastward moving signal in these fields. The characteristic zonal scale of the sea level pressure fluctuations, as estimated from the more limited phase information provided in Fig. 2d, is larger than that of the velocity potential fields. An additional feature worth noting in the sea level pressure pattern is that, for a given meridian, the fluctuations in the deep tropics tend to lead those in the subtropics. The phase structure of the sea level pressure field is in general agreement with the observed results reported by Madden and Julian (1972, Fig. 4); whereas the phase information on the observed upper tropospheric zonal wind, as provided by Maruyama (1982, Fig. 4b), seems to imply a faster propagation speed than is suggested in the corresponding model pattern (Fig. 2c).

Patterns similar to those displayed in Fig. 2 have been constructed with the reference point being located elsewhere along the equatorial belt. Such results (not shown) indicate that the entire phase pattern simply moves along with the reference point, so that the phase relationships described earlier are still retained. The inferences drawn from Fig. 2, hence, are rather independent of the particular choice of the reference location.

4. Eigenvector analysis

The results presented in section 3 clearly establish the presence in the model atmosphere of eastward propagating, global-scale phenomena with periods of about 20–40 days. It is seen that the signal is strongest for the divergent flow field, as represented by the velocity potential, less strong in the sea level pressure data, and marginally detectable in the 200 mb zonal wind. The velocity potential field is hence selected for further diagnosis in this section. Here an attempt is made to determine whether the oscillations described in Fig. 2 account for a sizeable fraction of the total variability. For this purpose we shall make use of empirical orthogonal function (EOF) techniques, which offer a concise representation of the principal modes of variability in terms of a few spatial patterns (eigenvectors) and time series (coefficients). In the present application, the EOF's are constructed using unfiltered 5-day averages of 205 mb velocity potential with the climatological seasonal cycle removed. The spatial grid analyzed has a resolution of 22.5° and 13.5° in the zonal and meridional directions, respectively, and extends from 74.25°S to 74.25°N.

The distributions of the eigenvectors for the four leading EOF's are shown in Fig. 3. We shall henceforth use the labels EOF1, EOF2, EOF3 and EOF4 to refer to both the temporal and spatial characteristics of these four principal modes. These EOF's, respectively, explain 27.9, 23.4, 7.7 and 6.8% of the globally integrated, nonseasonal variance. Note that EOF1 and EOF2 (Fig. 3a, b), which together account for over half of the total variance, both exhibit zonal wavenumber-1 patterns, with maximum amplitudes near the equator. The longitudinal phase difference between EOF1 and EOF2 is approximately one-quarter of a wavelength. EOF3 and EOF4 (Fig. 3c, d) are characterized by zonal wavenumber-2 features, with the longitudinal phase shift again being equal to a one-quarter wavelength.

The apparent quadrature relationships between EOF1 and EOF2, and between EOF3 and EOF4, are suggestive of phase propagation. This inference may be tested by subjecting the time series (coefficients) associated with those EOF's to cross-spectral analysis. The phase and coherence were obtained by applying the lag-correlation method and 20 lags were used. In Fig. 4 are shown the spectral distribution of squared coherence (curves) and phase difference (dots) between fluctuations of the coefficients for (a) EOF1 and EOF2, and for (b) EOF3 and EOF4. The threshold squared coherence values corresponding to the 95 and 99% significance levels are 0.26 and 0.32, respectively (see Panofsky and Brier, 1958; Julian, 1975). The evidence presented in Fig. 4a indicates that temporal variations in EOF1 and EOF2 are strongly coherent for a broad spectral band encompassing periods from 20 to 40 days, with EOF1 lagging EOF2 by one-quarter (90°) of a time period. This temporal lag, together with the lon-

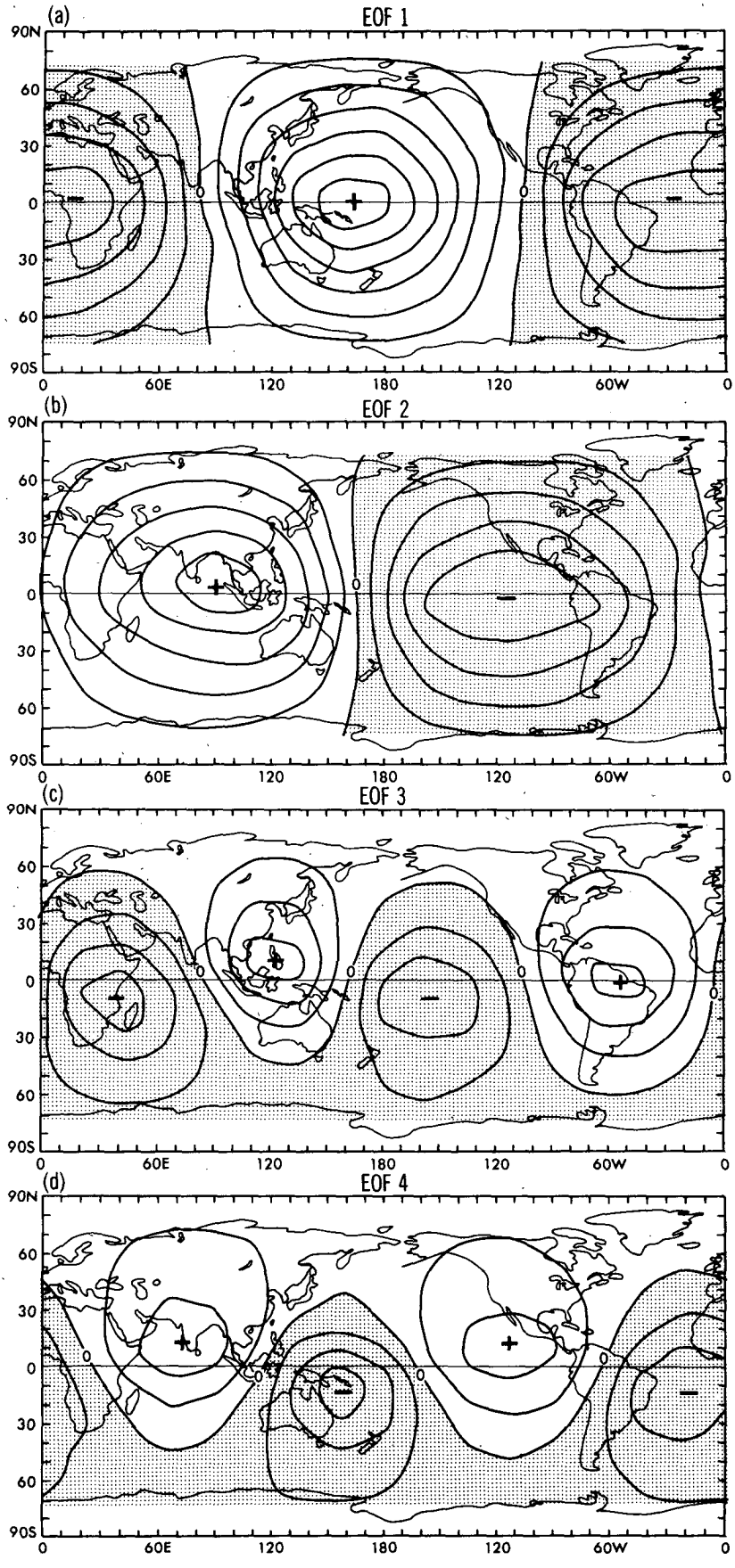
χ 205mb
(a)
EOF 1
(b)
EOF 2
(c)
EOF 3
(d)
EOF 4
90N
60
30
0
30
60
90S
0
60E
120
180
120
60W
0

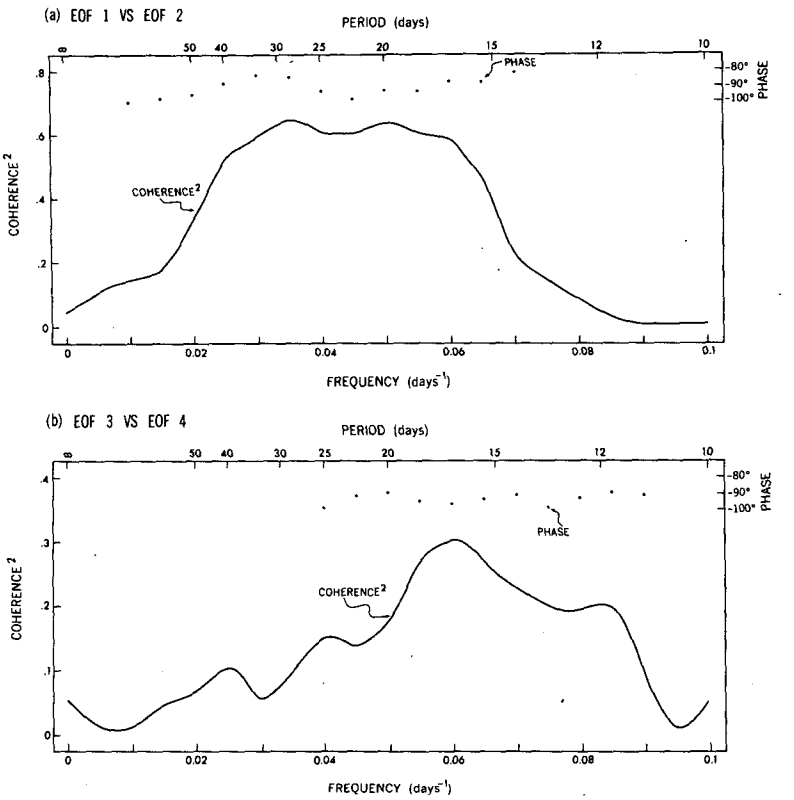

FIG. 4. Frequency dependence of the squared coherence (curves) and phase difference (dots) between (a) EOF1 and EOF2, and between (b) EOF3 and EOF4. Negative phase differences in panels (a) and (b) indicate EOF2 leading EOF1, and EOF4 leading EOF3, respectively.

gitudinal displacement between EOF1 and EOF2 (see Fig. 3a, b), constitute additional evidence that the eastward propagating, zonal wavenumber-1 oscillation discussed in section 3 is indeed the dominant mode of spatial and temporal variability of the large-scale divergent flow. Power spectra of the temporal coefficients of EOF1 and EOF2 (not shown) are also characterized by a primary peak within the frequency band corresponding to periods between 25 and 40 days. The typical period of the model-generated phenomena is hence seen to be slightly shorter than observed. We shall hereafter use the label "25–40 day oscillations" interchangeably with the simulated wavenumber-1 phenomena associated with EOF1/EOF2. Analogously, inspection of Figs. 3c, d and 4b reveals the presence of eastward traveling, zonal wavenumber-2 fluctuations, with squared coherence peaking at about 15–20 days. However, the temporal coherence between EOF3 and EOF4 is seen to be considerably weaker than that between EOF1 and EOF2.

A similar EOF analysis has also been performed using velocity potential data at 830 mb. The results (not shown) are almost identical to those displayed in Figs. 3 and 4. Hence these eastward propagating, wavenumber-1 and wavenumber-2 phenomena are discernible through the entire depth of the troposphere. Furthermore, it has been found using cross-spectral analysis that, for a given location, velocity potential fluctuations associated with the leading EOF's at 205 mb are almost exactly 180° out of phase relative to the corresponding fluctuations at 830 mb. Thus, large-scale divergence in the lower troposphere tends to be accompanied by large-scale convergence directly aloft, and vice versa.

The findings reported in this section are consistent with an EOF analysis performed earlier by Lorenc (1984) using velocity potential data for the FGGE year. This observational study has also identified eastward propagating oscillations with wavenumbers 1 and 2 as the principal modes of variability throughout the FGGE year. The characteristic time scales of the sim-

FIG. 3. Distributions of the (a) first, (b) second, (c) third, and (d) fourth eigenvectors of the 205 mb velocity potential (χ) field, as computed using unfiltered 5-day averages for the entire 12-year period with the seasonal cycle removed. Arbitrary units. Shading indicates negative values.

ulated wave modes are comparable to the observed values.

5. Spatial structure and temporal evolution of tropical oscillations associated with EOF1/EOF2

a. Selection of cases for constructing composites

A composite method is henceforth used to describe the typical three-dimensional structure and life-cycle of the zonal wavenumber-1 phenomena noted in sections 3 and 4. In view of the strong spatial and temporal coherence of the oscillations in the velocity potential field (Figs. 2a and 2b), as well as the significant fraction of total variance explained by the leading pair of eigenvectors in this field (Figs. 3a and 3b), the temporal coefficients associated with EOF1 and EOF2 constitute a convenient basis for identifying those time periods when the phenomena of interest are particularly active. The episodes thus selected can then be superposed to reveal the typical circulation features accompanying the 25–40 day oscillations.

Since we are primarily interested in those time scales associated with the wavenumber-1 phenomena, the raw coefficients for EOF1 and EOF2 were subjected to the bandpass (16–45 day) filter described in section 2 and Fig. 1. The variations of the filtered EOF coefficients through the 12-year period analyzed in this study are displayed in Fig. 5. The intermittent occurrence of quasi-cyclic behavior, with EOF2 leading EOF1 by one-quarter of a period, is evident from this plot. By careful inspection of Fig. 5, it is possible to choose the prominent episodes for constructing composites. This selection process is guided by the following criteria:

- The oscillations must be of sufficient amplitude to be distinguishable from the background noise.
- EOF1 and EOF2 must exhibit a quadrature relationship throughout each episode.
- The duration of each episode must be longer than one complete cycle.

The episodes thus chosen are indicated by shading in Fig. 5. These events encompass altogether 48 complete cycles, with 25 and 23 cycles occurring in the northern summer-half (April–September) and winter-half (October–March) of the calendar year, respectively.

In order to delineate the circulation features occurring in individual stages of the oscillations, the model data for a given episode are further partitioned ac-

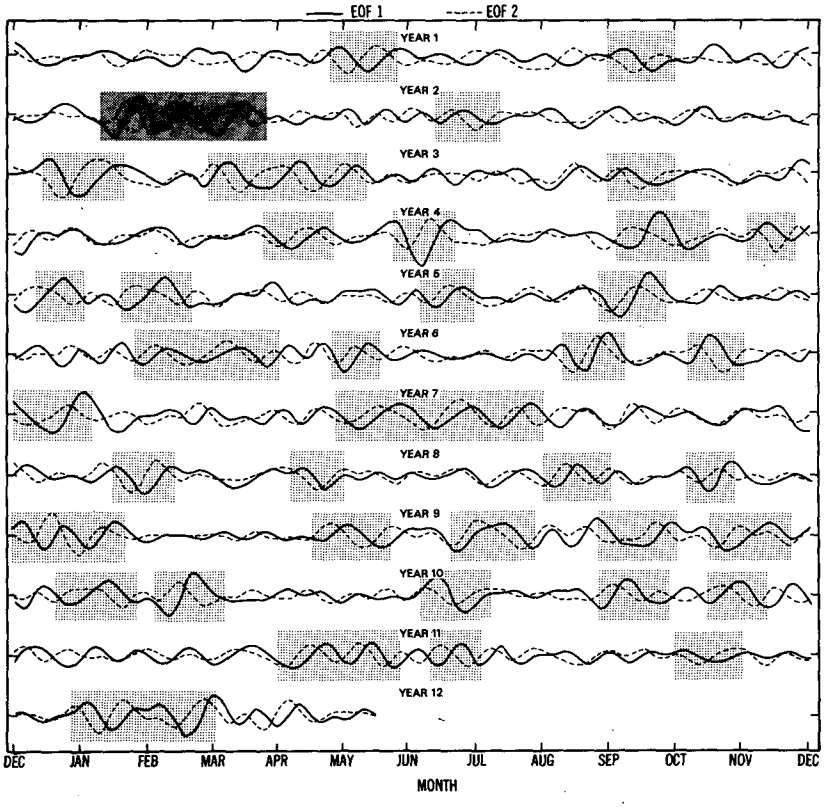

FIG. 5. Time series of the bandpass (16–45 days) filtered coefficients of EOF1 (solid curves) and EOF2 (dashed curves). Arbitrary units. Shading indicates active episodes used for constructing composites. Heavy shading in year 2 indicates the time period depicted by the phase diagram in Fig. 6.

cording to the temporal phase in that episode. This is achieved by examining phase diagrams, in which the x- and y-coordinates depict the variations of the coefficients for EOF1 and EOF2, respectively. The temporal phase at a certain time instant is hence represented by a point in such a diagram. The phase variation in the course of each episode chosen for constructing composites is depicted by the trajectory connecting the phase points for consecutive 5-day periods. An example of such a trajectory is shown in Fig. 6, which portrays the sequence of three oscillations occurring in the January–March period of year 2 (indicated by dark shading in Fig. 5). It is seen that, as time advances, this particular trajectory turns about the origin in a clockwise fashion, completing three revolutions in approximately 80 days. The clockwise rotation is again indicative of prevalent eastward phase propagation.

In the present composite procedure, four phase categories are defined as follows:

- Category 1: when the trajectory in the phase diagram intersects with the positive x-axis;
- Category 2: when the trajectory intersects with the negative y-axis;
- Category 3: when the trajectory intersects with the negative x-axis;
- Category 4: when the trajectory intersects with the positive y-axis.

Under this classification scheme, categories 1 and 4 correspond to those periods when the longitudinal phases of the velocity potential fluctuations coincide with those depicted in the patterns of EOF1 (Fig. 3a) and EOF2 (Fig. 3b), respectively, whereas categories 2 and 3 correspond to periods when the longitudinal phases are shifted by 180° relative to those in categories 4 and 1, respectively. These categories hence portray the four successive stages of the eastward traveling phenomena as they complete one circuit around the earth, with each stage being separated from the next by approximately 90° of longitude (or, equivalently, one-quarter of the time period). By examining phase diagrams for every active episode indicated by shading in Fig. 5, all time periods within the 12-year duration

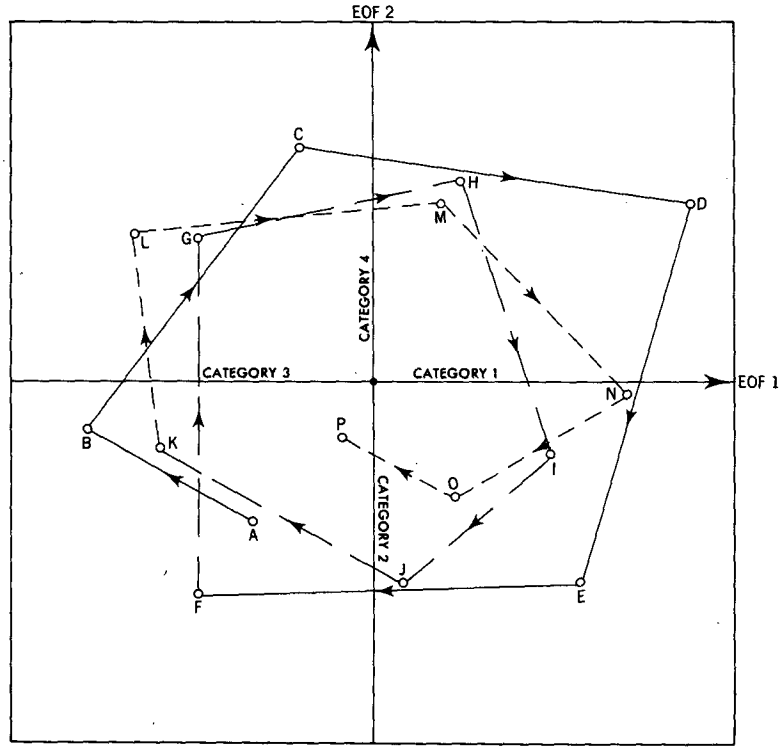

FIG. 6. Phase diagram for the January–March period of year 2 (see heavy shading in Fig. 5). The x- and y-coordinates are used to represent the temporal variations of EOF1 and EOF2, respectively. The amplitude and phase of the EOF1/EOF2 mode for each 5-day period is depicted by a point in the phase diagram. Straight lines are drawn to link pairs of points corresponding to successive 5-day periods. The points A and P correspond to the first and last 5-day periods in the time interval considered here, respectively. The intermediate 5-day periods are labelled chronologically in an alphabetical order. The first, second and third cycles of the oscillations are indicated by trajectories with solid line segments, long dashes and short dashes, respectively. Phases corresponding to categories 1–4 defined in the text are also shown.

which correspond to each of the four categories may be identified. Model data for all dates belonging to a certain category are then averaged to yield composites. Linear interpolations between pairs of consecutive 5-day means are used to estimate the data values on the dates when intersections between trajectories and the coordinate axes in the phase diagrams take place.

b. Horizontal structure

In Fig. 7 are shown the composite charts for categories 1–4 of the velocity potential field at (panel a) 205 and (panel b) 830 mb, as obtained using the procedure outlined above. In this study, the velocity potential function is defined such that the divergent com-

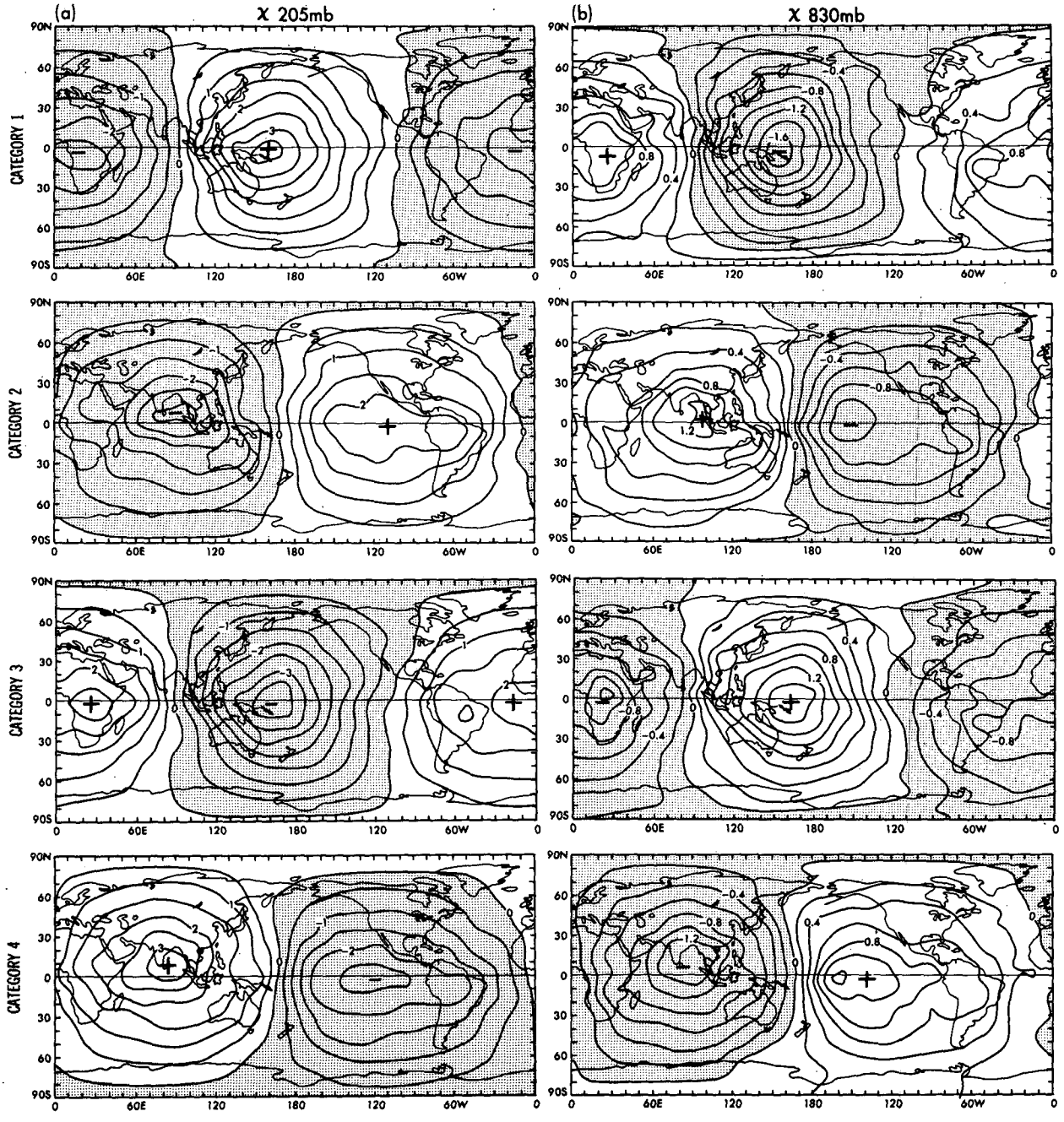

FIG. 7. Composite charts for categories 1–4, as constructed by superposing bandpass (16–45 day) filtered data for the velocity potential field at (a) 205 and (b) 830 mb during all active periods indicated in Fig. 5. Contour intervals for panels (a) and (b) are 5×10^5 m^2 s^{-1} and 2×10^5 m^2 s^{-1}, respectively. Shading indicates negative values. The divergent component of the motion field is directed perpendicular to the velocity potential contours towards higher values.

ponent of the motion field is directed from low velocity potential to high velocity potential. The composites in Fig. 7, as well as those to be shown in Figs. 8–15, are based on bandpass (16–45 day) filtered values (see section 2). Model data for all active episodes in the 12-year duration have been used in constructing the composites in Fig. 7, and no distinction among seasons was made. The systematic eastward phase propagation of the wavenumber-1 signal at both levels, as well as the 180° out of phase relationship between the upper and lower levels, are evident from Fig. 7. Inspection of Fig. 7 also reveals that, throughout much of the life cycle of these tropical oscillations, the most intense divergent flows (as inferred from the steepness of the velocity potential gradients) are located over Indonesia and the equatorial western Pacific. For comparison with circulation features to be presented later, we note here that category 2 corresponds to enhanced large-scale upper tropospheric divergence over the Indonesia-Indian Ocean sector, and convergence over the tropical eastern Pacific. The reverse situation is seen to prevail in category 4.

The composite charts for horizontal wind are displayed in Fig. 8 for (panel a) 205 and (panel b) 830 mb. Within the equatorial zone, fluctuations in the zonal wind component are seen to be much stronger than those in the meridional component. The 25–40 day oscillation appears in these patterns as an eastward traveling pair of easterly and westerly patches separated from each other by about 180° of longitude. These patches of zonal wind tend to be centered at the equator, and retain a notable degree of spatial coherence through the entire life cycle. The amplitude of the wind oscillations near the equator is about 3 and 1 m s^{-1} in the upper and lower levels, respectively. Away from the equator, the signal is seen to weaken considerably, and the oscillation is barely discernible near 30°N and 30°S. Comparison between Figs. 8a, b indicates that a strong negative correlation exists between the local zonal wind variations at the upper and lower levels.

The evolution of the 205 mb geopotential height and sea level pressure fluctuations associated with EOF1/EOF2 is illustrated by the composite charts displayed in Fig. 9. Both patterns are characterized by eastward moving, wavenumber-1 scale features confined within 15° of latitude from the equator. The amplitudes of these fluctuations are approximately 6 m for 205 mb height, and 0.5 mb for sea level pressure. Such equatorial perturbations tend to be accompanied by disturbances of the opposite polarity in locations farther north and farther south. Also apparent in Fig. 9 is the tendency for surface lows to be coincident with high centers in the upper tropospheric flow directly aloft, and vice versa. Comparison between the wind composites (Fig. 8) and the pressure composites (Fig. 9) at the corresponding level suggests that the strongest westerly (easterly) perturbations along the equatorial zone tend to be located slightly east of the strongest positive (negative) pressure perturbations.

Composite charts similar to Figs. 7–9 have also been plotted based on episodes for northern winter only and for northern summer only. These seasonal charts (not shown) bear a strong resemblance to the patterns presented in this subsection. Hence, the essential tropical circulation features associated with EOF1/EOF2 do not exhibit a strong seasonal dependence.

The statistical significance of the features noted in Figs. 7–9 has also been assessed by the Student's *t*-test. The approximate threshold values at the 95% confidence level for equatorial perturbations in 205 mb velocity potential, 830 mb velocity potential, 205 mb zonal wind, 830 mb zonal wind, 205 mb height and sea level pressure are respectively 1×10^6 m^2 s^{-1}, 5×10^5 m^2 s^{-1}, 1.5 m s^{-1}, 0.5 m s^{-1}, 3 m and 0.2 mb. Since most of the extrema appearing in Figs. 7–9 exceed these limits, the circulation features noted in these charts are significant departures from the long-term model climatology.

c. *Vertical structure*

The interrelationships among fluctuations at different pressure levels in the troposphere are illustrated in Fig. 10, which shows in a more compact format longitudinal variations of different composite quantities averaged over the 4.5°S–4.5°N latitudes, for (panel a) category 2 and (panel b) category 4. At a given longitude, the tendency for polarities of geopotential height, zonal wind and divergence fluctuations in the upper troposphere to be opposite to the corresponding fluctuations in the lower troposphere is again evident from this figure. It is also seen that negative and positive pressure perturbations at the surface are accompanied by positive and negative tropospheric thickness fluctuations, respectively. The strongest convergence of the zonal wind vectors at 830 mb is located slightly to the west of the surface low, and precipitation changes tend to be negatively correlated with the horizontal divergence at 830 mb. The data presented in Fig. 10 again illustrate the spatial phase relationship between the zonal wind and pressure (or geopotential height) fluctuations at the same level, as was noted earlier in the composite charts (Figs. 8 and 9).

The overall vertical structure of the circulation associated with EOF1/EOF2, as portrayed in Fig. 10 for the model tropics, is consistent with the schematic flow structure deduced by Madden and Julian (1972, Fig. 16) from observational data.

d. *Temporal evolution*

The temporal behavior of various circulation features during a typical life cycle of the tropical oscillations is depicted in Fig. 11, in which the composite data for zonal wind at (panel a) 205 and (panel b) 830 mb, (panel c) precipitation rate, (panel d) geopotential height at 205 mb, (panel e) sea level pressure, and (panel f) 1000–205 mb thickness are plotted as a function of

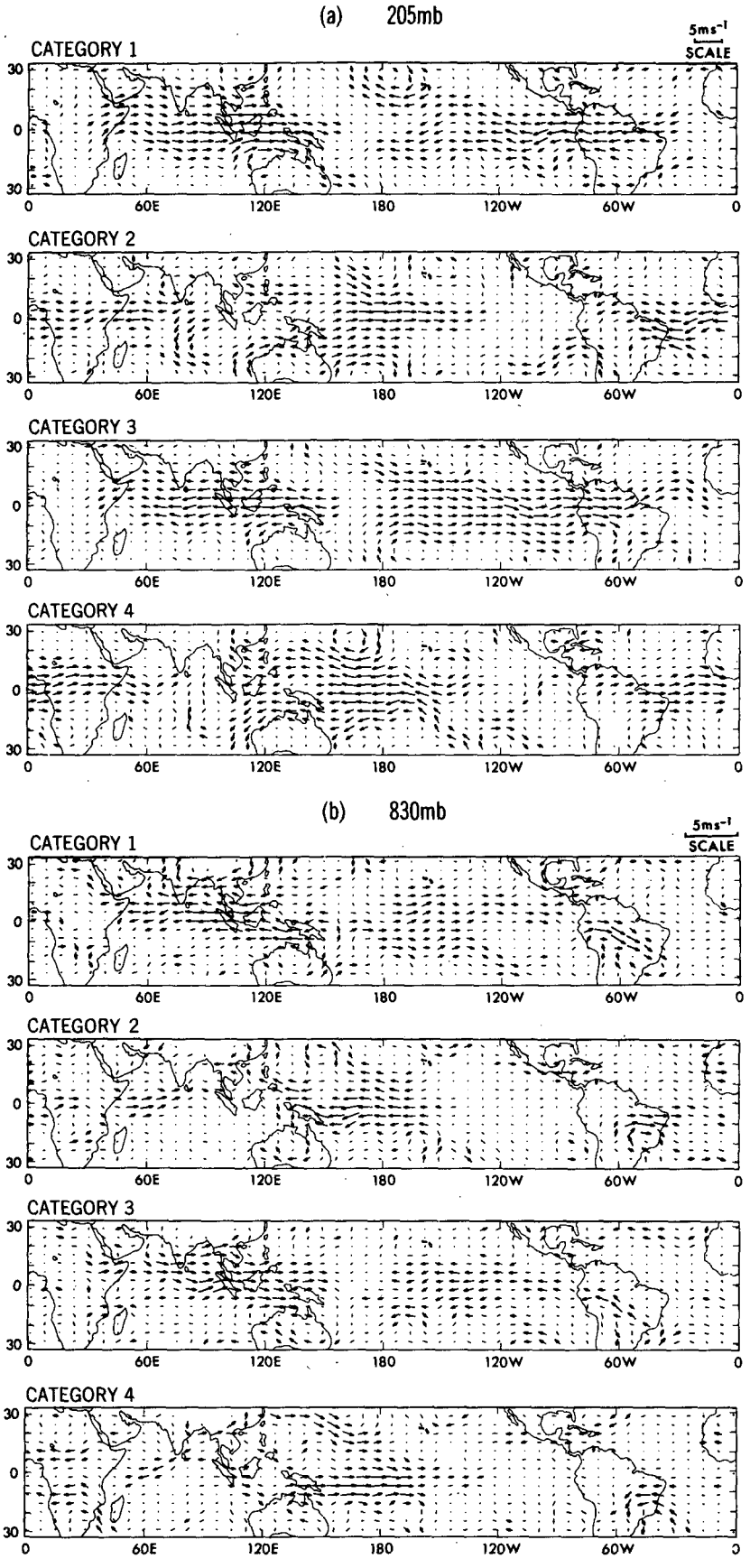

FIG. 8. As in Fig. 7, but for horizontal wind vectors; plotted according to the scale shown in the upper right.

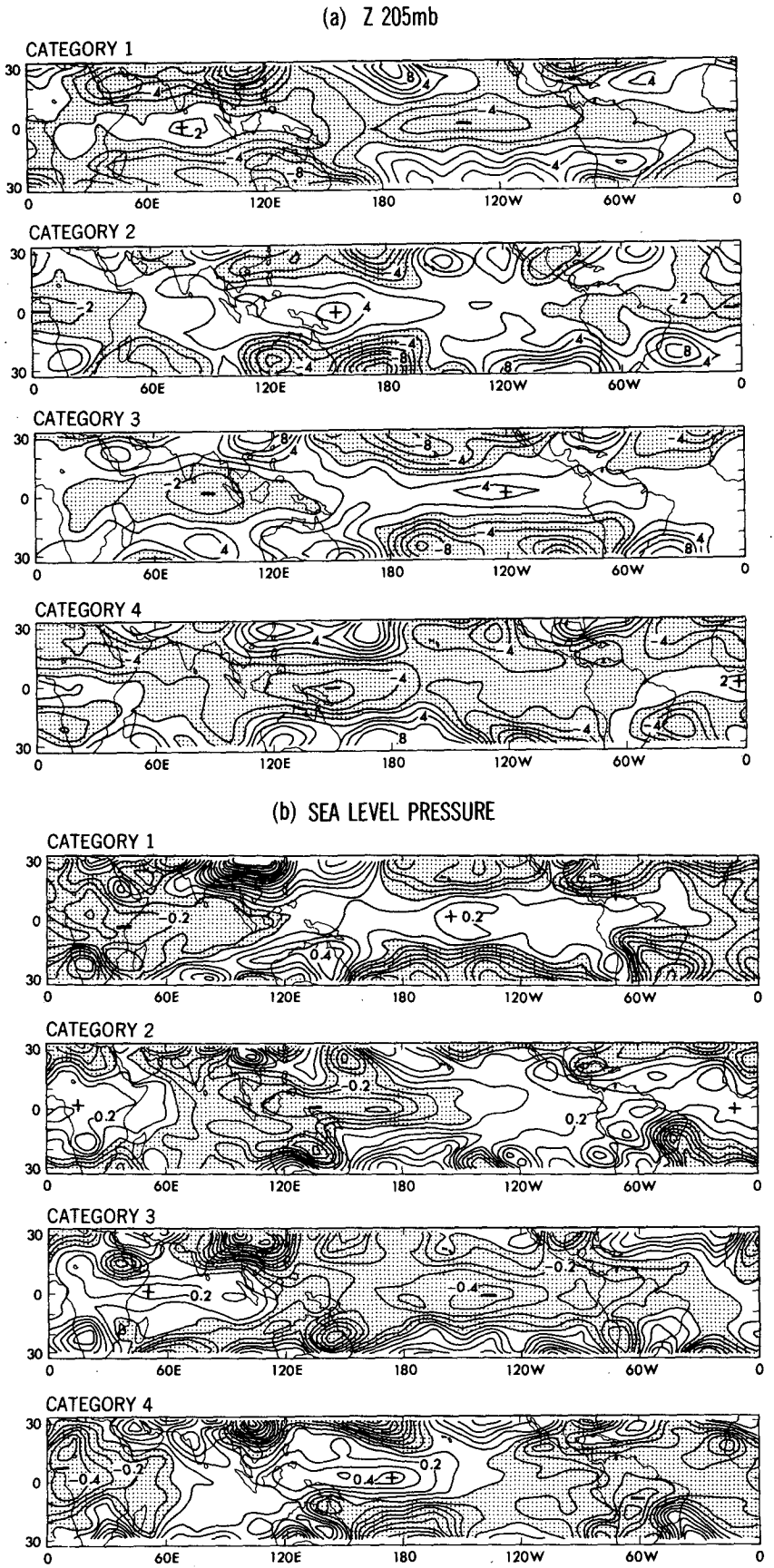

FIG. 9. As in Fig. 7, but for (a) 205 mb geopotential height and (b) sea level pressure. Contour intervals for panels (a) and (b) are 2 m and 0.1 mb.

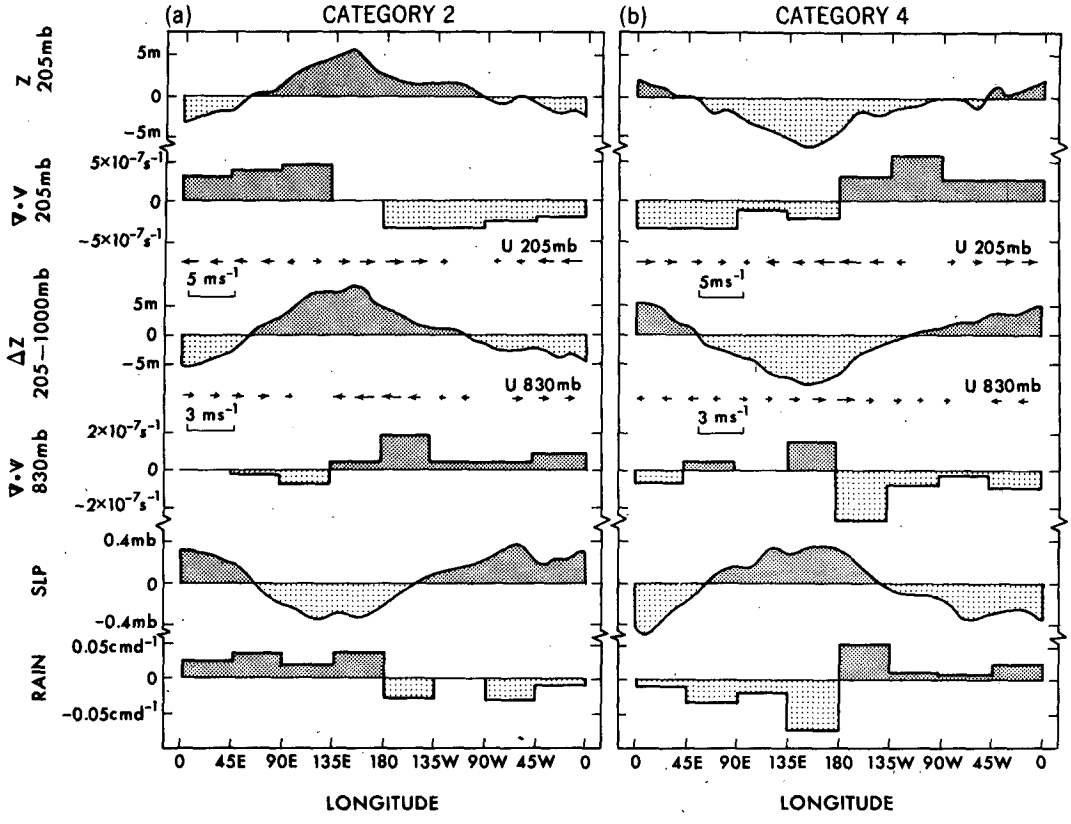

FIG. 10. Longitudinal variations of geopotential height, two-dimensional horizontal divergence and zonal wind (arrows) at 205 mb, 1000–205 mb thickness, zonal wind (arrows) and horizontal divergence at 830 mb, sea level pressure and precipitation rate, as obtained using bandpass (16–45 day) filtered values averaged between 4.5°S and 4.5°N, for (a) category 2 and (b) category 4. The arrows for the zonal wind composites are plotted according to the scale shown at the lower left.

time category and longitude. The values shown here are averages over the 4.5°S–4.5°N latitudes. With the exception of the precipitation field in panel c, the Hovmöller diagrams displayed in Fig. 11 provide further evidence of a well-defined signal which propagate eastward with an almost uniform phase speed of ~15 m s^{-1} through the entire cycle of the oscillation. It is also seen that the strongest amplitudes are attained within the longitudinal sector extending eastward from 90°E to 90°W.

The evolution of the precipitation composite (Fig. 11c) is less organized, and the overall eastward propagation speed appears to be lower than that for the other variables shown in Fig. 11. The most prominent features are located within 45° of longitude east and west of the date line. A positive extremum occurring at 155°E in category 2 is seen to drift slowly eastward and arrives at 160°W a half-period later. In category 2, the precipitation pattern in the equatorial Pacific appears as an east–west oriented dipole, with positive rainfall perturbations west of the date line being accompanied by negative perturbations farther east. As can be seen from Fig. 7, this category is characterized by large-scale 205 mb divergence and 830 mb convergence over the Indonesia-Indian Ocean sector, and by 205 mb convergence and 830 mb divergence over the eastern portion of the equatorial Pacific. In category 4, the polarities of the dipole-like structure in both the precipitation and velocity potential composites are opposite to those in category 2.

6. Seasonally dependent circulation features associated with EOF1/EOF2

Whereas the gross characteristics of the composite results described thus far are applicable throughout the year, there is nonetheless evidence that certain model phenomena associated with EOF1/EOF2 appear only during specific seasons. These seasonally dependent aspects of the 25–40 day oscillations are delineated by examining the Northern Hemisphere summertime composites and wintertime composites separately. The seasonal composites to be shown in this section have been constructed by superposing those active episodes (see Fig. 5) occurring in April–September (northern summer) only and in October–March (northern winter)

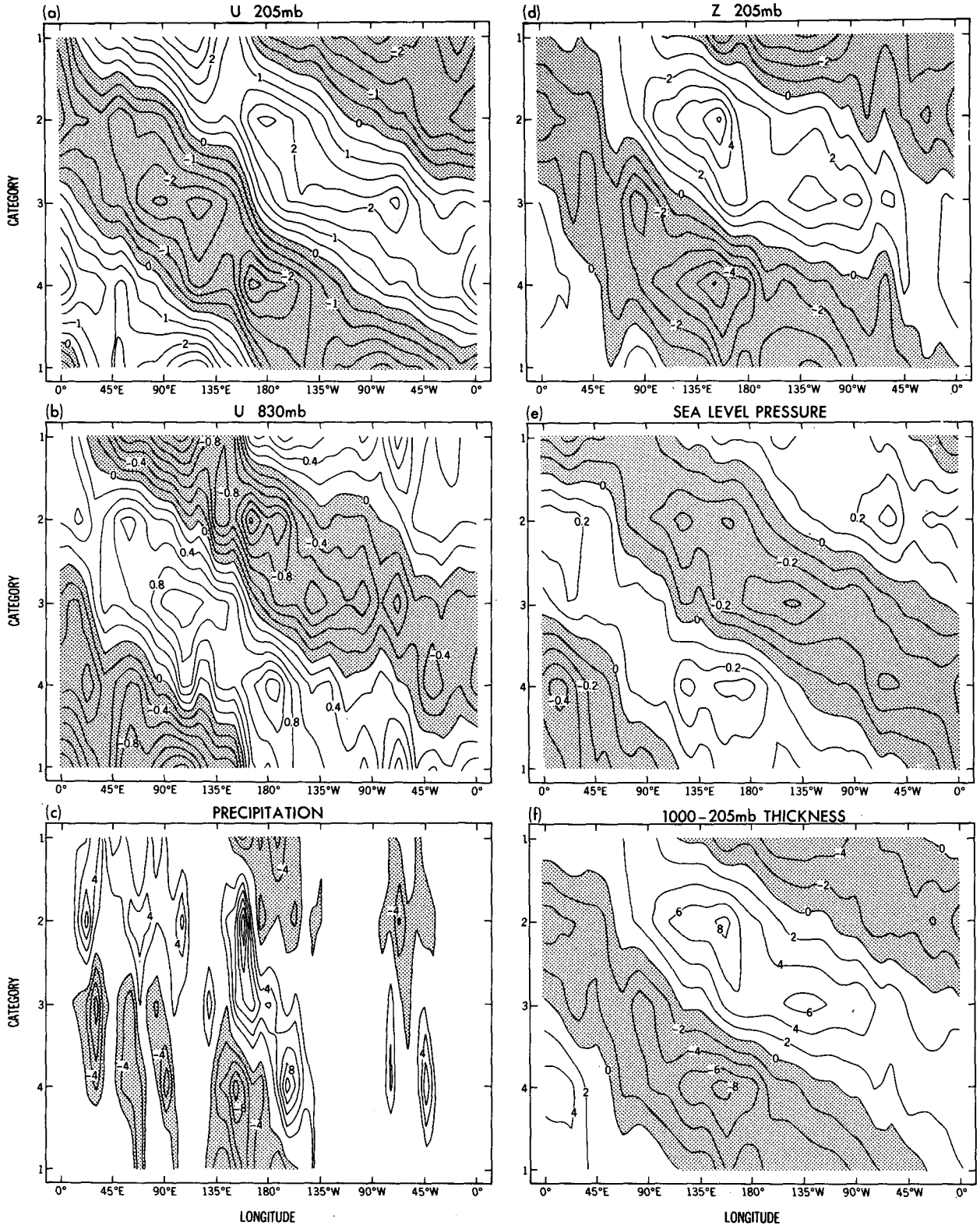

FIG. 11. Time category–longitude distributions of (a) 205 zonal wind, contour interval 0.5 m s^{-1}; (b) 830 mb zonal wind, contour interval 0.2 m s^{-1}; (c) precipitation rate, contour interval 0.02 cm d^{-1}; (d) 205 mb height, contour interval 1 m; (e) sea level pressure, contour interval 0.1 mb; and (f) 1000–205 mb thickness, contour interval 2 m; obtained using bandpass filtered values averaged between 4.5°S and 4.5°N. Shading indicates negative values. Note that the zero contour is omitted in panel c.

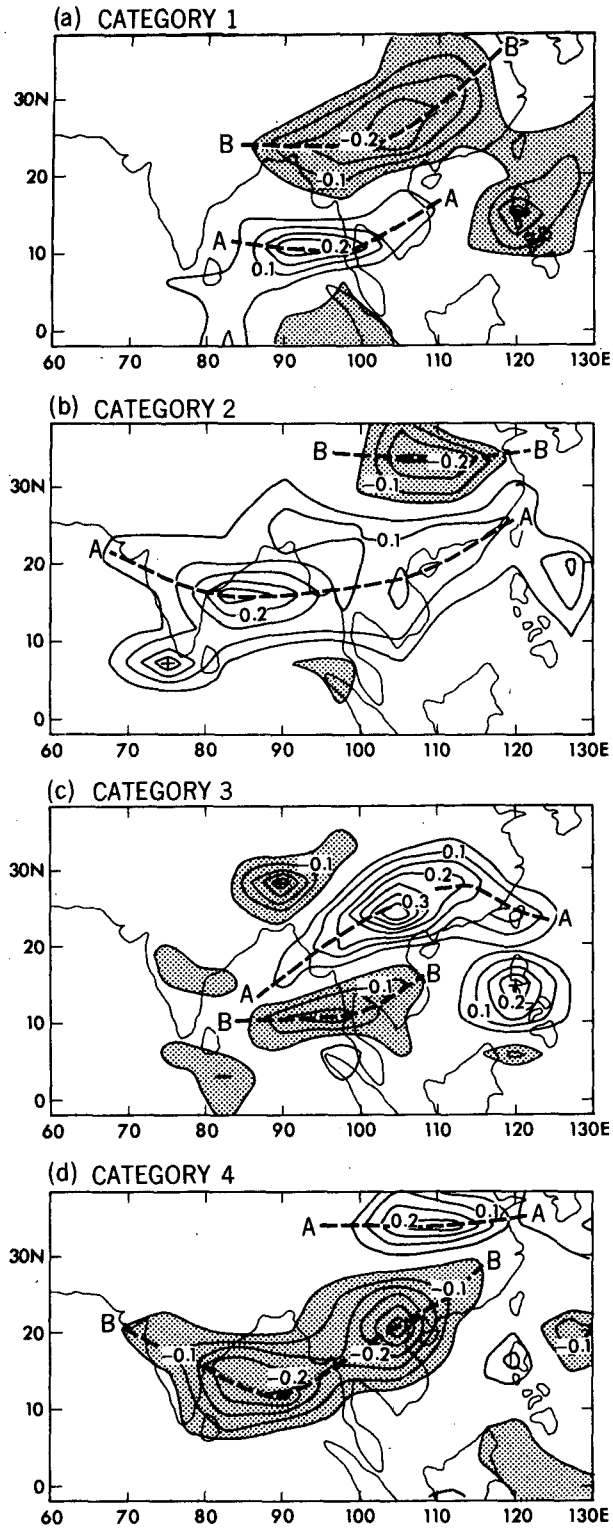

FIG. 12. As in Fig. 7, but for precipitation rate over the summer monsoon region in South Asia, as obtained based on active episodes occurring in the northern summer (April–September) only, for (a) category 1, (b) category 2, (c) category 3, and (d) category 4. Contour interval 0.05 cm d^{-1}. Shading indicates values less than −0.05 cm d^{-1}. The zero contour is omitted for the sake of clarity. The positions of the elongated bands of enhanced and suppressed precipitation in different categories are indicated by dashed lines with labels A and B, respectively.

only. As in section 5, all results shown here are based on bandpass filtered values using the procedures described in section 2.

a. Precipitation over the Asian summer monsoon region

In Fig. 12 are shown the summertime precipitation composites for South Asia during the time categories 1–4, as defined using the composite procedure outlined in section 5. It is evident from this figure that the summertime precipitation changes associated with EOF1/EOF2 are organized in a succession of zonally elongated bands over South Asia. Comparison between the patterns for different categories reveal a distinct tendency for these rainbands to migrate northward or northeastward with time. The propagation of these features is exemplified by the evolution of the pair of wet and dry belts labelled in the individual panels as "A" and "B", respectively. The precipitation belt A, which originates from the southern portion of the Bay of Bengal during category 1 (Fig. 12a), is seen to expand during category 2, covering much of eastern India, Indo-China and the south China coast (Fig. 12b). This feature reaches southwest China and undergoes considerable intensification there during category 3 (Fig. 12c), and is finally situated over central China during category 4 (Fig. 12d), thereby traversing altogether ~20° of latitude during its life history. The movement of the dry belt B is analogous to that of A, as may be appreciated by tracking the former feature starting from category 3 and proceeding sequentially to categories 4, 1 and 2.

Results from the Student's t-test (not shown) indicate that the threshold values of rainfall fluctuations corresponding to the 90 and 95% significance levels are 0.03 and 0.04 cm d^{-1}, respectively. These limits are generally exceeded by the precipitation rates along the axes of the rainband A and dry belt B in Fig. 12; we hence conclude that these are statistically significant features. The continuous, northward migration of the composite rainfall anomalies is also discernible in individual events, particularly within the 100°–130°E sector. This finding is therefore not merely an artifact of the composite procedure employed here.

The model features displayed in Fig. 12 are reminiscent of the train of northward propagating, east–west oriented trough and ridge lines noted by Krishnamurti and Subrahmanyam (1982, Fig. 3) during the summer Monsoon Experiment of FGGE. The observational results indicate that these troughs and ridges extend across the Indian Subcontinent towards the Arabian Sea, whereas the strongest precipitation bands in the model atmosphere are located over the Indo-

Chinese Peninsula and southwest China, with considerably weaker signals west of 80°E. More recently, Lau and Chan (1986) have noted the occurrence of a northward progression of wet and dry belts over South China in association with the onset of Mei-Yu ("Plum Rain") observed in that region. The pattern for category 3 (Fig. 12c) resembles the EOF pattern shown in their study based on OLR data. However, the east–west dipole in convective activity observed over India and the western subtropical Pacific (see Lau and Chan, 1986, Fig. 7) is much less evident in the model result.

The meridional propagation of the simulated rainbands is further illustrated by Fig. 13, in which the summertime composite precipitation data averaged over the 67.5°–120°E longitudes are plotted as a function of time category and latitude. Evident from this plot is the northward migration of the precipitation maxima and minima at an average speed of ~1.5 m s^{-1}. The pattern of Fig. 13 and the deduced propagation speed are consistent with the observed cloudiness data presented in a similar format by Yasunari (1980, Fig. 3). The latter study suggests that the convective activity originates near the equator, while the corresponding model results place the southernmost latitude of the precipitation bands at about 10°N.

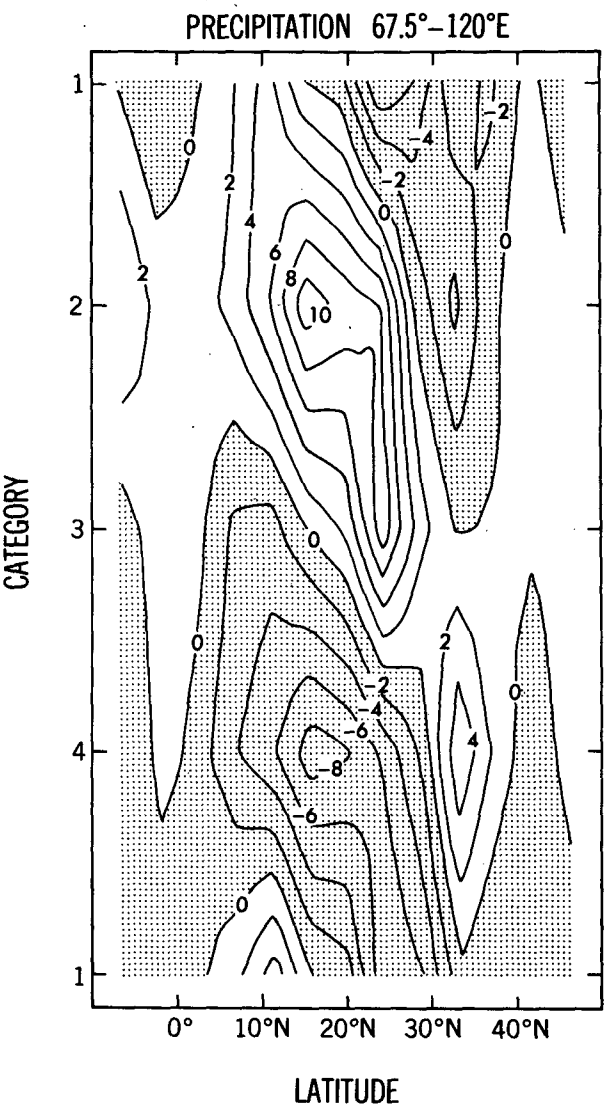

FIG. 13. Time category–latitude distribution of precipitation rate, as obtained by averaging bandpass (16–45 day) filtered values within the 67.5°–120°E sector for the northern summer (April–September) only. Contour interval 0.02 cm d^{-1}. Shading indicates negative values.

b. Extratropical wave activity in the wintertime Northern Hemisphere

Perturbations of the midlatitude circulation in the wintertime Northern Hemisphere associated with EOF1/EOF2 are portrayed in Fig. 14, which shows the distributions during winter of the 205 mb height composite for (panel a) category 1 and (panel b) category 3. The statistical significance of these patterns may be assessed by noting that the threshold values corresponding to the 95% confidence level increase from ~15 m for the zonal belt between 20° and 45°N, to ~30 m for regions located north of 60°N. The statistically significant centers of action in Fig. 14 appear to be organized in two well-defined wave trains. One of these wave trains is mostly situated over the Eurasian land mass, and extends from the European sector of the Arctic southeastward to eastern China. The horizontal tilt of the individual ridge and trough axes associated with this wave train is indicative of equatorward energy propagation. The second wave train is located in the Western Hemisphere, and is composed of centers over the subtropical Pacific, the Aleutian Islands, northern Canada and the eastern seaboard of the United States. This wave train is characterized by poleward energy propagation over much of the Pacific, and by equatorward energy propagation in regions farther east. It is seen that the polarity at individual centers in category 1 (Fig. 14a) is opposite to that at the same centers in category 3 (Fig. 14b). The corresponding composite patterns for categories 2 and 4 (not shown) are characterized by much weaker amplitudes and less distinct organization. The temporal evolution of the composite patterns in categories 1–4 also reveal no systematic phase propagation of the individual features. Hence the phenomena described in Fig. 14 seem to be geographically fixed perturbations with stationary nodes and antinodes. In view of the rather crude temporal resolution used here, with the typical time interval between adjacent categories being as much as 5–10 days, it is not feasible to determine whether the model-simulated wave trains exhibit the dispersive behavior observed for fluctuations with 10–30 day periods (Blackmon et al., 1984b). Composite charts based on 515 mb as well as 830 mb data (not shown) bear a strong resemblance to the 205 mb patterns in Fig. 14,

Z 205mb

(a) CATEGORY 1

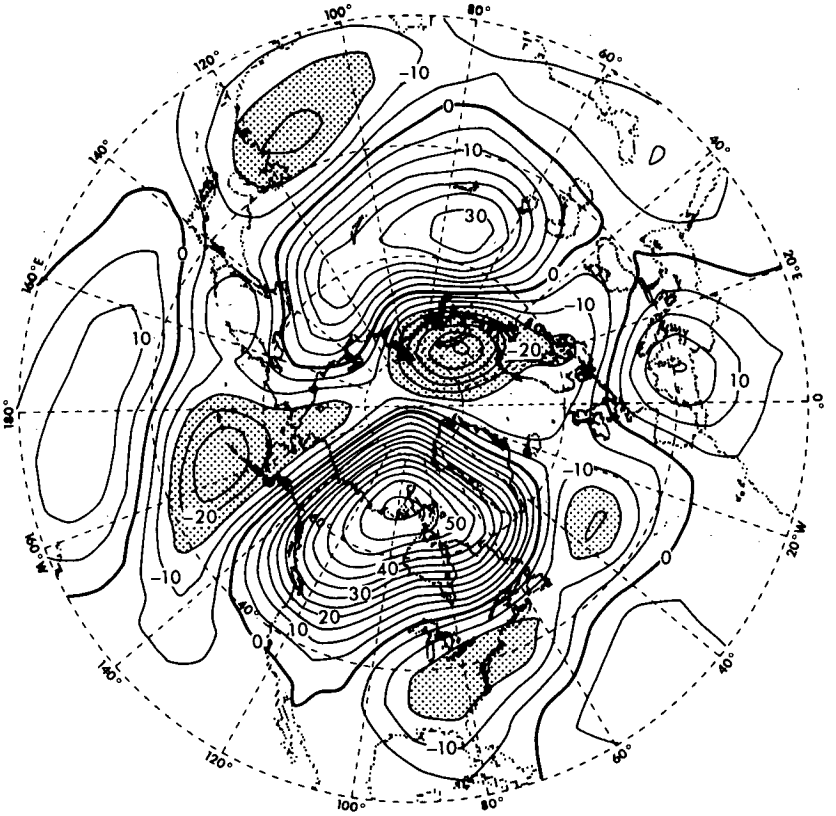

(b) CATEGORY 3

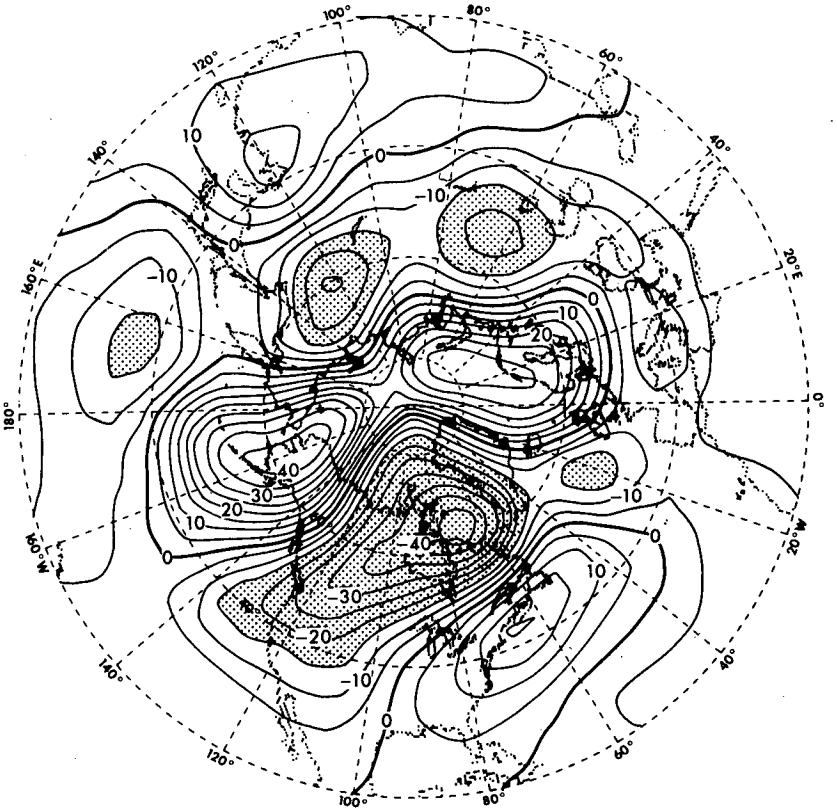

thus inferring an equivalent barotropic structure for the extratropical oscillations in much of the troposphere.

The recurrent circulation patterns in the observed wintertime Northern Hemisphere have been investigated by Wallace and Gutzler (1981) by applying cross-correlation techniques to monthly mean data. Two of the characteristic teleconnection maps identified therein, namely the Pacific/North American pattern (their Fig. 16) and the Eurasian pattern (their Fig. 25) may be compared with the composites shown in Fig. 14 of the present paper, and a considerable degree of similarity between model and observational results is noted. Furthermore, the observed teleconnection charts as well as the pertinent temporal correlation statistics (see Wallace and Gutzler, 1981, Figs. 16, 17, 25 and 27b, and Table 4) lend support to the model result that the Pacific/North American wave train tends to coexist with the Eurasian wave train. By analyzing observational records of 500 mb height and outgoing longwave radiation, Lau and Phillips (1986) and Knutson and Weickmann (personal communication, 1986) have shown that the space/time evolution of the observed Pacific/North American and Eurasian wave trains is coherent with tropical convection over the Indian and western Pacific oceans on intraseasonal time scales. The approximate quarter-period temporal lag between the simulated extratropical wave patterns (with amplitudes peaking in categories 1 and 3; see Fig. 14) and the tropical convective activity over the Indonesia/equatorial Pacific sector (with amplitudes peaking in categories 2 and 4; see Figs. 10 and 11c) is consistent with the findings reported by Lau and Phillips. In associating the simulated extratropical wave activities with tropical convection, we emphasize here that the pertinent precipitation signal (Fig. 11c) is not characterized by uniform propagation around the entire equatorial zone, but is instead largely confined to the western and central Pacific, with strongest rainfall occurring near 155°E and 160°W in categories 2 and 4, respectively.

Composite charts analogous to those in Fig. 14 have also been constructed using data for Northern Hemisphere summer, as well as for Southern Hemisphere summer and winter. These results (not shown) generally yield much weaker patterns, with little or no evidence of the geographically fixed fluctuations apparent in the Northern Hemisphere winter.

c. Seasonal displacement in the preferred location of near-equatorial zonal circulation cells

One of the distinct characteristics of the tropical circulation associated with EOF1/EOF2 is the tendency for the zonal wind at a given location in the lower troposphere to be directed opposite to that near the tropopause. (See Figs. 8, 10 and 11.) This relationship is illustrated in Fig. 15, which shows the temporal correlation coefficient between the zonal wind over a given grid point at 830 mb and the zonal wind over the same grid point at 205 mb. These charts have been obtained from bandpass filtered values (see section 2) for (panel a) northern summer and (panel b) northern winter. Data for entire seasons were used, so that the statistics displayed here pertain to the active as well as inactive periods identified in Fig. 5. The preferred sites of the zonal circulation cells should coincide with the axis of negative extrema in the tropical zone. Comparison between the patterns in Fig. 15a, b reveals that these preferred locations undergo systematic seasonal displacements, with a tendency for the most active zonal circulations to reside in the summer hemisphere. During the northern summer (Fig. 15a), the chain of minima lie along the 10°N latitude, with extreme values located over Central America and the summer monsoon region in South Asia. During the northern winter (Fig. 15b), this belt is centered at approximately 10°S, with minima appearing near New Guinea, central Brazil and the African region immediately south of the equator. Also evident from Fig. 15 is the prevalence throughout the year of strong positive correlations between the zonal flow at the upper and lower levels in the mid-latitude oceans, thus indicating predominantly equivalent barotropic circulations over those regions for fluctuations with 25–40 day time scales.

Recently Madden (personal communication, 1986) has computed coherence statistics beween the 850 and 150 mb zonal wind observed at 19 tropical radiosonde stations. His results indicate that the coherences at individual stations are strongest during the local summer season, and hence substantiate the seasonal migration of the simulated zonal circulation cells described here.

7. Behavior of tropical oscillations associated with EOF3/EOF4

The second pair of eigenvectors (EOF3/EOF4) presented in section 4 (Fig. 3c, d and 4b) indicate that, in addition to the zonal wavenumber-1 phenomenon described above, there also exists in the model atmosphere a relatively weaker wavenumber-2 component with a characteristic period of 15–20 days. In the present section, the properties of the smaller-scale features are documented by relating changes in various meteorological fields with changes in the temporal coefficients of EOF3 and EOF4. For this purpose, both the EOF coefficients and the model fields have been subjected

FIG. 14. Composite charts of 205 mb height for (a) category 1 and (b) category 3, as constructed using bandpass (16–45 day) filtered values for active episodes occurring in the northern winter (October–March) only. Contour interval 5 m. Shading indicates negative values less than −15 m. Latitude circles and meridians are drawn at 20° intervals. The outermost latitude circle is 20°N.

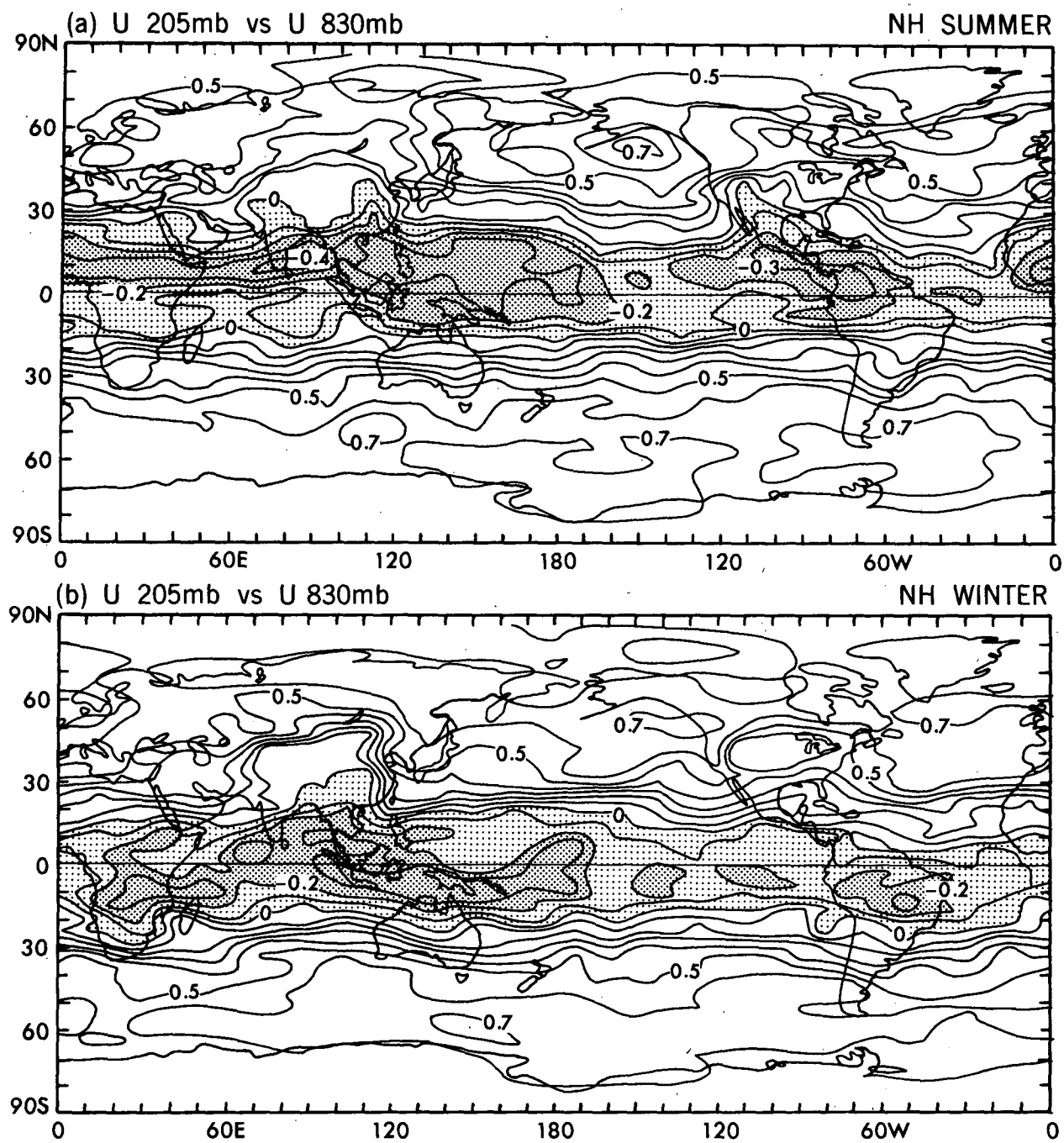

FIG. 15. Distributions of correlation coefficients between zonal wind at 205 mb and at 830 mb, as computed using all available bandpass (16–45 day) filtered data for (a) northern summer (April–September) only, and (b) northern winter (October–March) only. Contour interval 0.1. Shading indicates negative values.

to the high pass filter described in section 2, so that only fluctuations with periods shorter than 25 days are retained.

In Fig. 16 are shown the distributions of correlation coefficients between the 205 mb zonal wind at individual grid points and the coefficients for (panel a) EOF3 and (panel b) EOF4, as computed using all available high pass filtered 5-day averages during the 12-year period. The corresponding correlation charts based on zonal wind data at 830 mb are shown in panels c and d of the same figure. Noting the quarter-wavelength longitudinal phase difference between the patterns in Fig. 16a, b, and recalling the previous result (Fig. 4b) that the coefficients for EOF4 lead the coef-

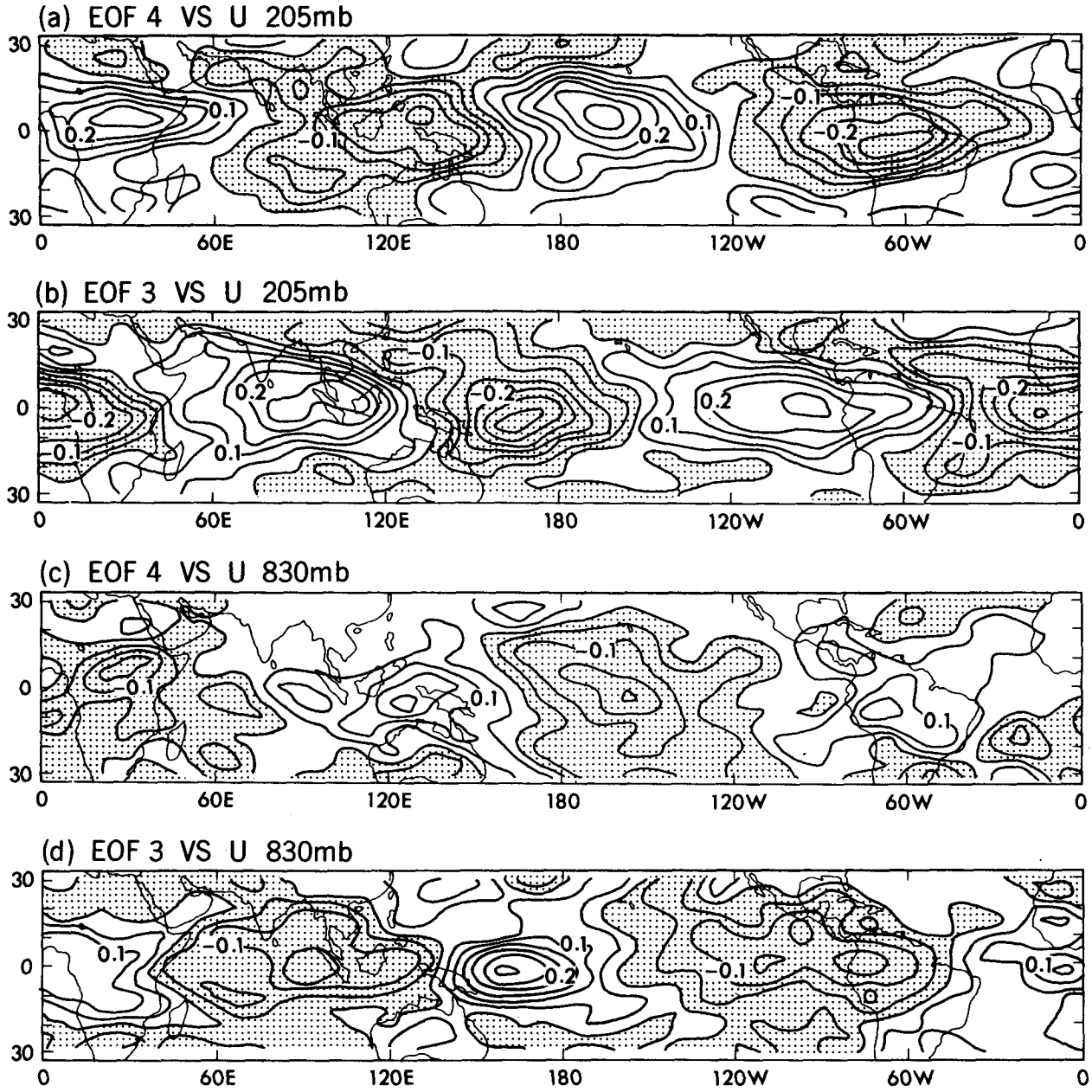

FIG. 16. Distributions of the correlation coefficients between grid point values of 205 mb zonal wind and coefficients of (a) EOF4 and (b) EOF3, and between grid-point values of 830 mb zonal wind and coefficients of (c) EOF4 and (d) EOF3, as computed using high pass filtered (<25 day) data for the entire 12-year period. Contour interval 0.05. Shading indicates negative values.

ficients for EOF3 by a quarter-period, the EOF3/EOF4 mode is seen to be associated with zonal wavenumber-2 oscillations in the equatorial 205 zonal wind field with an eastward phase speed of ~ 15 m s^{-1}. This propagation speed is almost identical to that associated with the wavenumber-1 phenomena described in the previous sections. The patterns obtained from 830 mb wind data (Fig. 16c, d) exhibit a strong negative spatial correlation with their counterparts for 205 mb data (Figs. 16a and 16b), thus suggesting that the EOF3/EOF4 oscillations are also characterized by circulation cells in the equatorial zonal plane, with easterlies lying over westerlies, and vice versa.

Correlation charts similar to Fig. 16 but constructed using 205 mb height and sea level pressure data are displayed in Fig. 17. The latter patterns are also dominated by an eastward traveling, wavenumber-2 signal in the equatorial zone. Also evident in Fig. 17 is the

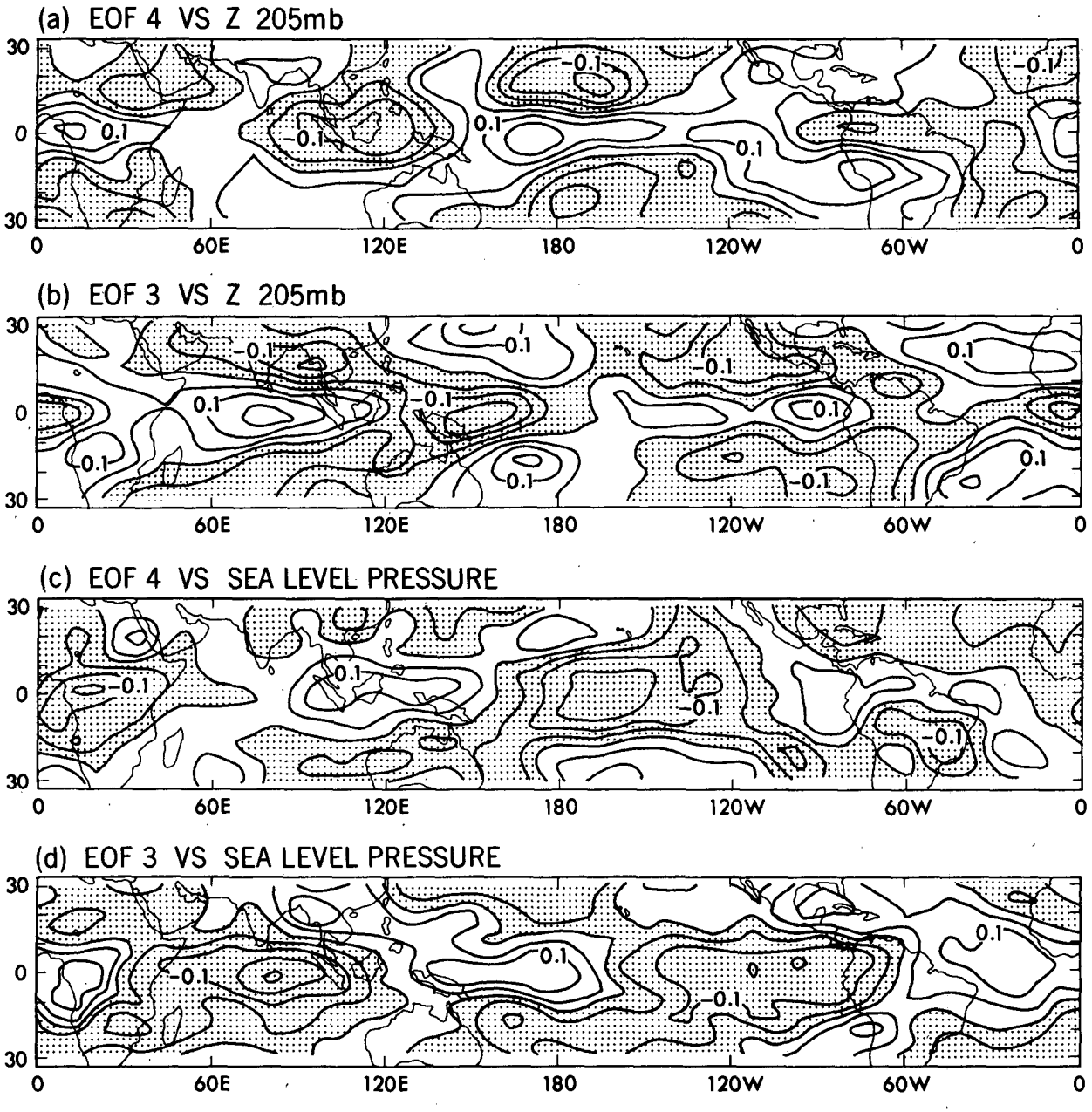

FIG. 17. As in Fig. 16, but for correlations of EOF coefficients with 205 mb height [panels (a) and (b)], and with sea level pressure [panels (c) and (d)].

negative correlation between the fluctuations in sea level pressure and those in the 205 mb height for the same grid point. Comparison between the corresponding panels in Figs. 16 and 17 reveals that the longitudinal phase for the zonal wind perturbations at 205 mb is related to that for the geopotential height at the same level, with the strongest westerlies (easterlies) being located just east of the strongest positive (negative) height fluctuations. A similar relationship is evident in the patterns for the near-surface zonal wind and sea level pressure.

In summary, except for the difference in zonal wavelength, the spatial structure and propagation speed of the circulation features associated with EOF3/EOF4 bear a strong resemblance to those associated with EOF1/EOF2. The strong similarities noted here further suggest that the four leading EOFs of the velocity potential field (Fig. 3) represent different aspects of essentially the same phenomenon. Fluctuations with zonal scales corresponding to both wavenumber-1 and (to a lesser extent) wavenumber-2 apparently contribute to this phenomenon. In analogy with Fourier anal-

ysis, the EOF approach employed here tends to decompose such contributions into two distinct pairs of eigenvectors.

8. Dynamical interpretation

Although the time scales (25–40 days) of the dominant low-frequency oscillations in the model are somewhat shorter than the 30–60 day time scales actually observed in the tropics, the spatial and temporal variation of the simulated oscillation and the associated extratropical teleconnections agree reasonably well with the observed. We believe that the present model has captured the essential physics of the 40–50 day oscillations noted in the observational literature. Thus, it is now possible to understand the mechanism(s) of these low-frequency oscillations in terms of the controlled environment of our GCM experiments. While further diagnosis is undoubtedly required, a preliminary assessment of the plausible mechanisms of the phenomenon is presented in the following subsections. Discussions pertaining to the basic mechanisms of the oscillation, its association with the monsoonal circulation, and tropical–extratropical interactions are presented separately.

a. Basic mechanisms

Since the model atmosphere has not been subjected to any external forcing with time scales of 25–40 days, the oscillations noted in this study with such time scales are apparently generated internally by the model dynamics and physics. The essential characteristics of the simulated 25–40 day oscillations, i.e., its zonal scale, direction and speed of propagation, warm-core monsoonal structure, as well as the discernible phase relationship between its associated zonal wind and pressure perturbations, bear some resemblance to the Kelvin wave modes predicted in the study by Chang (1977). [See also the correspondence between Stevens and White (1979) and Chang (1979)]. The latter theoretical finding depends crucially on the formulation of a linear damping term supposedly representing the dissipative effects of cumulus friction. We note here that no such mechanism has been explicitly parameterized in the GCM examined here, and that the tropical circulation in the model atmosphere is nearly inviscid. However, the diagnosis by Sardeshmukh and Held (1984) of another version of this GCM with a higher resolution indicates that the strong damping required by most linear studies to explain the tropical flow pattern might be viewed as compensating for the stationary nonlinearities and transient eddy mixing neglected in such studies, rather than depicting cumulus friction effects. Whereas the present model study does not allow for a definitive assessment of the importance of cumulus friction in the 25–40 day phenomenon, the robust signals in the simulated velocity potential field associated with this oscillation (Figs. 2–7) are nevertheless suggestive of a substantial role of tropical convection through its modulation of the divergent motion field.

An often-asked question regarding the 40–50 day oscillations concerns the role of the ocean in accounting for the preferred time scale. Since our experiment was carried out in the absence of any nonseasonal sea surface temperature perturbations, it appears that the climatological distribution of sea surface temperature only controls the geographical locations of the most intense convection, whereas the preferred 25–40 day time scale detected here is determined mainly by the interaction between moist convection and dynamical processes in the model atmosphere. Another factor of interest is the potential role of feedback processes involving perturbations in zonal wind and in evaporation near the air–sea interface. It is worth noting that 40–50 day signals have been found in many oceanographic parameters, e.g., surface current over the Indian Ocean (McPhaden, 1982); sea level in the coastal regions of South America (Enfield and Lukas, 1984) and sea surface temperature in the Somali current (Mysak and Mertz, 1984). The relationships between these features observed in the oceans and their counterparts in the atmosphere remain to be ascertained.

b. Association with the monsoonal circulation

Both our model results and observations indicate that while the eastward propagation of the intraseasonal modes are present throughout the year, there exists strong modulation of these modes by the seasonal cycle. The most notable example is the northward propagation of the successive wet and dry belts over East Asia and India during northern summer in association with the simulated 25–40 day oscillations (Figs. 12–13). These northward moving wave disturbances over the monsoon regions have also been simulated by Webster (1983) and Goswami and Shukla (1984) using zonally symmetric models. These studies illustrate that such circulation features might be produced through interactions between a variety of processes such as moist convection, surface hydrology, cloud-radiative feedback and atmospheric dynamics. We emphasize here that the cloud cover has been fixed in the present GCM experiment, hence the interaction between cloud amount and radiative processes does not appear to be essential for the formation of the northward migrating rainbands. The relevance of the remaining mechanisms proposed in these simplified models to the corresponding monsoonal features detected in the observed and GCM atmospheres may be clarified by diagnosing additional model integrations in which the mechanisms in question are not incorporated.

c. Tropical-extratropical interactions

Weickmann et al. (1985) have noted the occurrence of global modes of oscillation with 30–60 day time scales. The existence of extratropical wave trains as-

sociated with the tropical low-frequency oscillation found in our study provides further evidence of the extratropical and possibly global influence of the 40–50 day oscillations. An intriguing feature in the relationship between tropical convection and extratropical circulation is that the extratropical wave trains are in approximate quadrature with the strongest convective activity over the Indonesia-dateline sector. The wave train over Eurasia exhibits an equatorward energy propagation upstream of the Indonesia/dateline dipole heating pattern, whereas the wave train over Pacific/North America shows a poleward energy propagation downstream of the dipole heating pattern. Such a configuration is suggestive of mutual forcing with delayed response among tropical convection and midlatitude wave trains. With these interactive mechanisms in action, the 40–50 day oscillations in the tropics may actually be linked to extratropical normal modes with comparable time scales. One candidate of such low-frequency modes in the extratropics is that discerned by Simmons et al. (1983) in a theoretical study of two-dimensional barotropic instability.

9. Concluding remarks

We have analyzed the 12-year output of a 15-wavenumber GCM experiment with the objective of describing the spatial and temporal behavior of dominant intraseasonal variations. The parameters analyzed include 5-day averages of wind, geopotential height, sea level pressure and precipitation. The model results are compared with a large array of observational studies. It is demonstrated that a considerable degree of consistency exists between observed and simulated results on horizontal and vertical scales, propagation characteristics, seasonality, as well as three-dimensional patterns of the pressure and velocity perturbations associated with the phenomena of interest. The evidence presented here, being derived independently from a GCM integration, corroborates with the earlier findings of many observational works in establishing the 40–50 day oscillation as an important mode of atmospheric variability with global influences.

One of the keys to a comprehensive understanding of the 40–50 day oscillations appears to be the specific role of latent heating associated with moist convection in the model tropics, both in modulating the wave disturbances along the equatorial belt, and in interacting with the wintertime extratropical flow. Another issue of interest is the possible relationship between the 40–50 day oscillation and interannual variability of the tropical ocean-atmospheric system associated with the El Niño-Southern Oscillation, as suggested by Lau (1985). The latter, longer-term phenomenon involves strengthening and weakening of a Walker-type circulation over the equatorial Pacific. The zonal wind and precipitation anomalies accompanying such changes are reminiscent of those described in the present paper.

At this writing, an understanding of the intraseasonal oscillations appearing in different versions of the spectral GFDL GCM is being actively pursued. The findings of these ongoing investigations may be briefly summarized as follows:

- Tropical features associated with the 25–40 day oscillations are clearly discernible in a 48-month integration with a 15-wavenumber model devoid of ocean–continent contrast, orography and the seasonal cycle. Annual mean insolation has been prescribed throughout the experiment, and the lower boundary for the entire globe is assumed to be a smooth land surface which remains saturated. (See Held, 1983, section 6.7 for further details.) It hence appears that the occurrence of the low-latitude, intraseasonal phenomena described in the present paper is not crucially dependent on the presence of the climatological seasonal cycle, nor are the essential characteristics of such phenomena strongly influenced by spatial inhomogeneities at the lower boundary.
- The 25–40 day phenomena are also detected in another 15-year model experiment designed to study various features related to the El Niño-Southern Oscillation (ENSO). In that model run, the observed month-to-month sea surface temperature variations over the tropical Pacific for the period from 1962 to 1976 have been incorporated in the lower boundary condition. (See Lau, 1985 for further details.) This simulation hence offers a good opportunity for delineating the interdependence among the 2–5 year ENSO cycles and the much shorter-period fluctuations examined in the present study.
- Hayashi and Golder (personal communication, 1986) have analyzed the output of a single-summer integration using a higher-resolution GCM with rhomboidal truncation at 30 wavenumbers, as well as the Level III-B analyses for the FGGE summer. The space–time spectra for both observed and simulated zonal wind data are indicative of zonal wavenumber-1, eastward moving phenomena, with two spectral peaks of comparable power and corresponding to periods of 40–50 and 25–30 days, respectively. Hence the 30-wavenumber model is apparently capable of generating oscillations with somewhat longer time scales than those diagnosed in the 15-wavenumber model. The potential impact of model resolution (and perhaps also model physics) on the characteristic period of these intraseasonal phenomena, as well as the similarities and differences between the 40–50 day and the 25–30 day features identified in Hayashi and Golder's study, deserve further scrutiny.

Although much of the intraseasonal phenomena described here remain to be explained, it is evident from the wide array of model results outlined above that the GCM will serve as a valuable tool for addressing various outstanding issues.

Acknowledgments. We are indebted to S. Manabe and the Climate Dynamics Group at GFDL for developing and maintaining the GCM which provided the data for this study. We also thank M. L. Blackmon, Y. Hayashi, I. M. Held and A. H. Oort for offering constructive comments on an earlier version of the manuscript, and J. M. Wallace and T. R. Knutson for several helpful discussions on the results. The figures were prepared by the GFDL Scientific Illustration Group and J. Conner. The manuscript was typed by J. Kennedy.

REFERENCES

Blackmon, M. L., 1976: A climatological spectral study of the 500 mb geopotential height of the Northern Hemisphere. *J. Atmos. Sci.*, **33**, 1607–1623.

——, Y.-H. Lee and J. M. Wallace, 1984a: Horizontal structure of 500 mb height fluctuations with long, intermediate and short time scales. *J. Atmos. Sci.*, **41**, 961–979.

——, ——, —— and H-H. Hsu, 1984b: Time variation of 500 mb height fluctuations with long, intermediate and short time scales as deduced from lag-correlation statistics. *J. Atmos. Sci.*, **41**, 981–991.

Chang, C. P., 1977: Viscous internal gravity waves and low frequency oscillation in the tropics. *J. Atmos. Sci.*, **34**, 901–910.

——, 1979: Reply [to comments by Stevens and White]. *J. Atmos. Sci.*, **36**, 547.

Enfield, D., and R. Lukas, 1984: Low frequency sea level variability along the South American Coast during 1981–83. *Trop. Ocean-Atmos. Newslett.*, **28**, 2–4.

Goswami, B. N., and J. Shukla, 1984: Quasi-periodic oscillation in a symmetric general circulation model. *J. Atmos. Sci.*, **41**, 20–37.

Held, I. M., 1983: Stationary and quasi-stationary eddies in the extratropical troposphere: theory. *Large-Scale Dynamical Processes in the Atmosphere*, B. J. Hoskins and R. P. Pearce, Eds., Academic Press, 397 pp.

Julian, P. J., 1975: Comments on the determinations of significance levels of the coherence statistic. *J. Atmos. Sci.*, **32**, 836–837.

Knutson, T. R., K. M. Weickmann and J. E. Kutzbach, 1986: Global scale intraseasonal oscillations of outgoing longwave radiation and 250 mb zonal wind during Northern Hemisphere summer. *Mon. Wea. Rev.*, **114**, 605–623.

Krishnamurti, T. N., and D. Subrahmanyam, 1982: The 30–50 day mode at 850 mb during MONEX. *J. Atmos. Sci.*, **39**, 2088–2095.

——, P. K. Jayakumar, J. Sheng, N. Surgi and A. Kumar, 1985: Divergent circulations on the 30 to 50 day time scale. *J. Atmos. Sci.*, **42**, 364–375.

Lau, K. M., 1985: Elements of a stochastic dynamical theory of the long-term variability of the El Niño/Southern Oscillation. *J. Atmos. Sci.*, **42**, 1552–1558.

——, and P. H. Chan, 1985: Aspects of the 40–50 day oscillation during the northern winter as inferred from outgoing longwave radiation. *Mon. Wea. Rev.*, **113**, 1889–1909.

——, and ——, 1986: Aspects of the 40–50 day oscillation during the northern summer as inferred from outgoing longwave radiation. *Mon. Wea. Rev.*, **114**, in press.

——, and T. J. Phillips, 1986: Coherent fluctuations of extratropical geopotential height and tropical convection in intraseasonal time scales. *J. Atmos. Sci.*, **43**, 1164–1181.

Lau, N-C., 1981: A diagnostic study of recurrent meteorological anomalies appearing in a 15-year simulation with a GFDL general circulation model. *Mon. Wea. Rev.*, **109**, 2287–2311.

——, 1985: Modeling the seasonal dependence of the atmospheric response to observed El Niños in 1962–76. *Mon. Wea. Rev.*, **113**, 1970–1996.

Liebmann, B., and D. L. Hartmann, 1984: An observational study of tropical-midlatitude interaction on intraseasonal time scales during winter. *J. Atmos. Sci.*, *41*, 3333–3350.

Lorenc, A. C., 1984: The evolution of planetary-scale 200 mb divergent flow during the FGGE year. *Quart. J. Roy. Meteor. Soc.*, **110**, 427–441.

Madden, R. A., and P. R. Julian, 1971: Detection of a 40–50 day oscillation in the zonal wind in the tropical Pacific. *J. Atmos. Sci.*, **28**, 702–708.

——, and ——, 1972: Description of global-scale circulation cells in the tropics with a 40–50 day period. *J. Atmos. Sci.*, **29**, 1109–1123.

Manabe, S., and D. G. Hahn, 1981: Simulation of atmospheric variability. *Mon. Wea. Rev.*, **109**, 2260–2286.

Maruyama, T., 1982: Upper tropospheric zonal wind oscillation with a 30–50 day period over the equatorial western Pacific observed in cloud movement vectors. *J. Meteor. Soc. Japan*, **60**, 172–181.

McPhaden, M., 1982: Variability in the central equatorial Indian Ocean. Part I. Ocean dynamics. *J. Marine Res.*, **40**, 157–176.

Murakami, T., and T. Nakazawa, 1985: Tropical 45 day oscillations during the 1979 Northern Hemisphere summer. *J. Atmos. Sci.*, **42**, 1107–1122.

Mysak, L., and G. J. Mertz, 1984: A 40–60 day oscillation in the source region of the Somali current during 1976. *J. Geophys. Res.*, **89**, 711–715.

Panofsky, H. A., and G. W. Brier, 1958: *Some Applications of Statistics to Meteorology.* The Pennsylvania State University, 224 pp.

Sardeshmukh, P. D., and I. M. Held, 1984: The vorticity balance in the tropical upper troposphere of a general circulation model. *J. Atmos. Sci.*, **41**, 768–778.

——, and B. J. Hoskins, 1985: Vorticity balances in the tropics during the 1982–83 El Niño-Southern Oscillation event. *Quart. J. Roy. Meteor. Soc.*, **111**, 261–278.

Simmons, A. J., J. M. Wallace and G. W. Branstator, 1983: Barotropic wave propagation and instability and atmospheric teleconnection patterns. *J. Atmos. Sci.*, **40**, 1363–1392.

Stevens, D. E., and G. H. White, 1979: Comments on "Viscous internal gravity waves and low-frequency oscillations in the tropics." *J. Atmos. Sci.*, **36**, 545–546.

Wallace, J. M., and D. S. Gutzler, 1981: Teleconnections in the geopotential height field during the Northern Hemisphere winter. *Mon. Wea. Rev.*, **109**, 784–812.

Webster, P. J., 1983: Mechanics of monsoon low-frequency variability: surface hydrological effects. *J. Atmos. Sci.*, **40**, 2110–2124.

Weickmann, K. M., G. R. Lussky and J. E. Kutzbach, 1985: Intraseasonal (30–60 day) fluctuations of outgoing long wave radiation and 250 mb streamfunction during northern winter. *Mon. Wea. Rev.*, **113**, 941–961.

Yasunari, T., 1979: Cloudiness fluctuations associated with the Northern Hemisphere summer monsoon. *J. Meteor. Soc. Japan*, **57**, 227–242.

——, 1980: A quasi-stationary appearance of 30 to 40 day period in the cloudiness fluctuations during the summer monsoon over India. *J. Meteor. Soc. Japan*, **58**, 225–229.